

## Water Mass Transformation in Salinity–Temperature Space

MAGNUS HIERONYMUS, JOHAN NILSSON, AND JONAS NYCANDER

*Department of Meteorology, Stockholm University, Stockholm, Sweden*

(Manuscript received 28 November 2013, in final form 12 June 2014)

### ABSTRACT

This article presents a new framework for studying water mass transformations in salinity–temperature space that can, with equal ease, be applied to study water mass transformation in spaces defined by any two conservative tracers. It is shown how the flow across isothermal and isohaline surfaces in the ocean can be quantified from knowledge of the nonadvective fluxes of heat and salt. It is also shown how these cross-isothermal and cross-isohaline flows can be used to form a continuity equation in salinity–temperature space. These flows are then quantified in a state-of-the-art ocean model. Two major transformation cells are found: a tropical cell driven primarily by surface fluxes and dianeutral diffusion and a conveyor belt cell where isoneutral diffusion is also important. Both cells are similar to cells found in earlier work on the thermohaline streamfunction. A key benefit with this framework over a streamfunction approach is that transformation due to different diabatic processes can be studied individually. The distributions of volume and surface area in  $S$ – $T$  space are found to be useful for determining how transformations due to these different processes affect the water masses in the model. The surface area distribution shows that the water mass transformations due to surface fluxes tend to be directed away from  $S$ – $T$  regions that occupy large areas at the sea surface.

### 1. Introduction

The oceanic temperature<sup>1</sup>  $T$  and salinity  $S$  distributions result from an interplay between air–sea fluxes, large-scale circulation, and small-scale turbulent mixing. The extreme  $S$ – $T$  values are created by the surface fluxes of heat and freshwater (Speer 1993), whereas the turbulent mixing acts to reduce the span of the  $S$ – $T$  distribution. The large-scale circulation serves to bring water masses from different locations together, allowing the small-scale mixing to blend their properties.

As the salinity and temperature affect the density, their distributions are coupled in a nonlinear fashion to the ocean circulation. This fact makes the theory of the large-scale ocean circulation a challenging problem, but it also provides some constraints on the oceanic density distribution. These general constraints have been examined and exploited in dynamical oceanography. One

prominent example is the theory of the ventilated thermocline (Welander 1959; Luyten et al. 1983; Marshall and Nurser 1991), where conservation of potential vorticity connects the thermocline density distribution, along the isopycnal surfaces, to the conditions in the surface mixed layer. Another example is the advective–diffusive model for the abyssal ocean stratification (Munk 1966). Recently, elements of these two theoretical concepts have been incorporated into a model of the meridional overturning circulation and its associated stratification (Nikurashin and Vallis 2012).

Most of the dynamically based theories pertaining to the oceanic density distribution have been formulated in terms of a single buoyancy variable, rather than explicitly in temperature and salinity, fields that have different surface boundary conditions. This tends to complicate the theoretical analyses significantly. An alternative approach is to abandon the geographical coordinates and instead analyze how water masses are formed and maintained in  $S$ – $T$  coordinates. In this approach, the focus is on how the volumetric  $S$ – $T$  distribution,  $v(S, T, t)$ , of the World Ocean is affected by specific processes. In this context,  $v(S, T, t)dSdT$  specifies the volume of water in the World Ocean with a temperature and salinity within the small range  $dSdT$  around  $S$  and  $T$  (Worthington 1981). In classical oceanography, regional

<sup>1</sup>Note that in this manuscript, the variable referred to as temperature, denoted by  $T$ , is the potential temperature.

Corresponding author address: Magnus Hieronymus, Dept. of Meteorology, Stockholm University, Stockholm S-10691, Sweden.  
E-mail: magnus@misu.su.se

*S*–*T* relations, either from single hydrographic stations or ocean basins, have been an important tool for identifying water masses, circulation, and mixing (e.g., [Picard and Emery 1982](#)).

Several efforts have been made to relate processes that affect the temperature and salinity fields in the ocean to transformation of water masses. [Waln \(1977\)](#) presented a framework for describing a salinity-stratified ocean region using the salinity as an independent variable. Specifically, he derived relations for how the volumetric salinity distribution is affected by surface freshwater fluxes and mixing in the interior ocean. Based on similar ideas, [Waln \(1982\)](#) considered the distribution of water masses in temperature space, relating the rate of change of the temperature distribution to the air–sea heat flux and interior mixing. The results of [Waln \(1982\)](#) have been applied and extended in many subsequent studies and have also become a widely used diagnostic tool in ocean circulation modeling studies. For instance, Waln's ideas have been used to compute transformations between density classes ([Tziperman 1986](#); [Speer and Tziperman 1992](#); [Iudicone et al. 2008b](#)), to translate wind-induced entrainment into water mass transformation ([Nilsson 1996](#)), to examine how mixed layer processes and eddies affect water mass transformations ([Marshall 1997](#); [Marshall et al. 1999](#)), and to create transformation and formation maps, showing the geographical locations where water mass transformation and formation occur ([Brambilla et al. 2008](#); [Maze et al. 2009](#)).

In an interesting application, [Speer \(1993\)](#) showed how the ideas of Waln can be extended to describe water mass transformations due to air–sea fluxes in the *S*–*T* plane. He used this method to undertake an observationally based study of water mass transformation and formation in the North Atlantic. In that work, Speer introduced a transformation vector, which describes the strength and direction of the water mass transformation in the *S*–*T* plane. Recently, [Döös et al. \(2012\)](#) and [Zika et al. \(2012\)](#) introduced a different but somewhat related description of water mass transformations in *S*–*T* space. Their idea was to project the three-dimensional global ocean circulation onto a “thermohaline” *S*–*T* streamfunction, which describes the volume transport across a global isothermal (isohaline) surface as a function of salinity (temperature). This can be viewed as an extension of the representation of the meridional overturning circulation in latitude–potential density coordinates ([Bryan and Sarmiento 1985](#)), which generally yields a more Lagrangian description of the zonal-mean overturning than that obtained in latitude–depth coordinates ([Hirst et al. 1996](#)). As discussed by [Döös et al. \(2012\)](#) and [Zika et al. \(2012\)](#), although the thermohaline streamfunction lacks geographical coordinates, it

still delineates aspects of water mass transformations associated with the global interbasin ocean circulation as well as geographically distinguishable water mass transformations occurring in tropical and abyssal circulation cells.

Both [Döös et al. \(2012\)](#) and [Zika et al. \(2012\)](#) calculated their streamfunctions as time averages based on the instantaneous velocity field perpendicular to the isohaline and isothermal surfaces. Subsequently, [Groeskamp et al. \(2014\)](#) showed that there is an additional component to the total thermohaline streamfunction (which they called the diathermohaline streamfunction) that arises from correlations between the movements of the isothermal and isohaline surfaces associated with the seasonal cycle and the general time variability of the thermohaline forcing, which can cause these surfaces to move geographically even in the absence of ocean currents. Notably, [Groeskamp et al. \(2014\)](#) found that the time variability of the thermohaline forcing gives a significant contribution to the diathermohaline streamfunction, which describes the net water mass transformations in a statistically steady state. In effect, they calculated<sup>2</sup> the flow across an isothermal (or alternatively an isohaline surface, with corresponding modifications) caused by the material rate of change of temperature, that is,

$$\frac{DT}{Dt} = \frac{\partial T}{\partial t} + \mathbf{u} \cdot \nabla T = -\nabla \cdot \boldsymbol{\phi}_T,$$

where  $\mathbf{u}$  is the velocity, and  $\boldsymbol{\phi}_T$  is the nonadvectional heat flux. [Döös et al. \(2012\)](#) and [Zika et al. \(2012\)](#) based their *S*–*T* streamfunctions only on the advective part of the material rate of change, that is, the term  $\mathbf{u} \cdot \nabla T$  (or correspondingly  $\mathbf{u} \cdot \nabla S$  for the cross-isohaline flow). The difference between these two streamfunctions is discussed in detail by [Groeskamp et al. \(2014\)](#) but also discussed formally in appendix B.

In the present work, we extend the ideas of [Speer \(1993\)](#), [Döös et al. \(2012\)](#), [Zika et al. \(2012\)](#), and [Groeskamp et al. \(2014\)](#) by making a formal description of the ocean water mass transformation in *S*–*T* coordinates. This effort is essentially a straightforward generalization of [Waln \(1977\)](#) and [Waln \(1982\)](#) to include both *S* and *T* simultaneously. Moreover, by following Waln and focusing on the right-hand side of the equation above and its counterpart for salinity, this approach allows us to examine separately water mass transformations due to surface fluxes and various interior mixing processes. Furthermore, we can establish

---

<sup>2</sup>[Kjellsson et al. \(2014\)](#) used the same approach to calculate a static energy–latent energy streamfunction in the atmosphere.

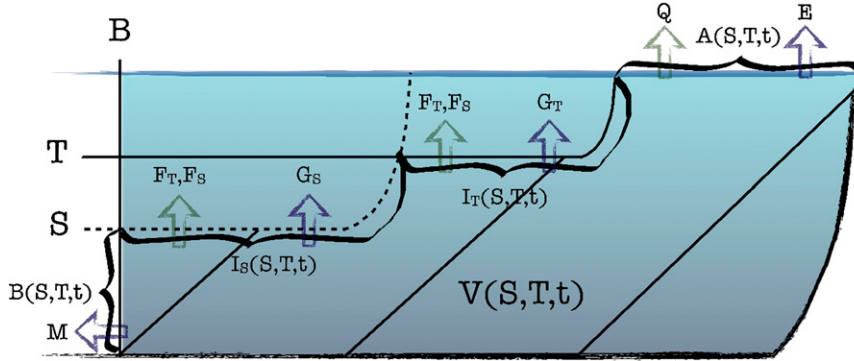


FIG. 1. Sketch of the oceanic region  $V(T, S, t)$  (the region filled with sloping lines) where the salinity is less than  $S$ , and the temperature is less than  $T$  and its boundaries. Those are  $I_S$ ,  $I_T$ ,  $A$ ,  $B$ , and the thick black line that is the sea floor and ocean sidewall. Green arrows indicate nonadvective fluxes of heat and salt and blue arrows indicate volume fluxes.

the formal connection between the transformation vector and the diathermohaline streamfunction. Specifically, we formulate relations that connect the time rate of change of  $v(S, T, t)$  to the surface fluxes and the small-scale mixing. This provides a quantitative framework for describing processes controlling the global water mass distribution, an element that was not provided in the earlier studies (Speer 1993; Döös et al. 2012; Zika et al. 2012; Groeskamp et al. 2014).

We will then go on to illustrate a few applications of this framework by analyzing a near-steady-state ocean model simulation of the global ocean circulation. Our focus will be to examine the role of transformations due to surface fluxes, lateral (isoneutral) mixing, and vertical (dianeutral) mixing for the maintenance of a steady water mass distribution in the global ocean. In this effort, we will examine the balances between the formation and destruction of a few of the key water masses in the ocean and also attempt to trace formation and destruction occurring in the  $S$ - $T$  coordinates back to the geographical regions where the actual surface fluxes and mixing occur.

## 2. Definitions and basic relations

Here, we derive relations describing the time evolution of the volumetric  $S$ - $T$  distribution, which follow from conservation of mass, heat, and salt. We use the Boussinesq approximation, under which conservation of mass is replaced by conservation of volume, which is given by the continuity equation

$$\nabla \cdot \mathbf{u} = 0, \quad (1)$$

where  $\mathbf{u}$  is the velocity. Heat conservation is given by

$$c \frac{\partial T}{\partial t} = -\nabla \cdot (cT\mathbf{u} + \boldsymbol{\phi}_T), \quad (2)$$

where  $T$  is potential temperature,  $c = \rho_r c_p$  is the constant heat capacity per unit volume,  $\rho_r$  is a constant reference density, and  $\boldsymbol{\phi}_T$  is the nonadvective heat flux. Salt conservation is given by

$$\frac{\partial S}{\partial t} = -\nabla \cdot (S\mathbf{u} + \boldsymbol{\phi}_S), \quad (3)$$

where  $S$  is salinity and  $\boldsymbol{\phi}_S$  is the nonadvective salt flux.

Following ideas of Walin (1982), we introduce a function  $V(S, T, t)$  that specifies the volume of water in the ocean (or a subregion of the ocean) having a salinity less than or equal to  $S$  and a temperature less than or equal to  $T$ . We also define fluxes of volume, heat, and salt that act to change the state variable  $V(S, T, t)$  and derive some useful relationships between these fluxes.

### a. Definitions

We consider a region in the ocean bounded by the sea surface, the sea floor, and an internal vertical boundary  $B$  (see Fig. 1). We introduce the following variables and flows describing the state and evolution of the water properties in the region of consideration:

$V(S, T, t)$ : volume of water having a salinity less than  $S$  and a temperature less than  $T$

$A(S, T, t)$ : the sea surface area, including sea ice covered regions, where the salinity is less than  $S$  and the temperature less than  $T$

$I_T(S, T, t)$ : the part of the isothermal surface  $T$  where the salinity is less than  $S$

$I_S(S, T, t)$ : the part of the isohaline surface  $S$  where the temperature is less than  $T$

$G_T(S, T, t)$ : the volume flow penetrating the isothermal surface  $I_T(S, T, t)$ , counted positive when leaving the region

- $G_S(S, T, t)$ : volume flow penetrating the isohaline surface  
 $I_S(S, T, t)$ , counted positive when leaving the region  
 $M(S, T, t)$ : the volume flow having a salinity less than  $S$  and a temperature less than  $T$  that exits through the interior control surface  $B$   
 $E(S, T, t)$ : net volume flow of freshwater exiting across the surface  $A(S, T, t)$ , that is, evaporation minus precipitation, net ice melt, and runoff from land  
 $Q(S, T, t)$ : the net sea surface heat flux out of  $A(S, T, t)$ .  
 $F_T(S, T, t)$ : the diffusive heat flux through the surfaces  $I_T(S, T, t)$ ,  $I_S(S, T, t)$ , and  $B$ , counted positive when leaving the region  
 $F_S(S, T, t)$ : the diffusive salt flux through the surfaces  $I_T(S, T, t)$ ,  $I_S(S, T, t)$ , and  $B$ , counted positive when leaving the region

The function  $V(T, S, t)$  has a direct connection to the volumetric  $S$ - $T$  distribution, which specifies the volume of water in a certain salinity and temperature interval (Worthington 1981). The volume in the temperature and salinity range from  $T$  to  $T + dT$  and  $S$  to  $S + dS$  is  $v(S, T, t) dSdT$ , defined as

$$v(S, T, t) \equiv \frac{\partial^2 V}{\partial T \partial S}. \quad (4)$$

---


$$c \frac{\partial}{\partial t} \int_{T_{\min}}^T T' \frac{\partial V}{\partial T'} dT' = -cTG_T - \int_{T_{\min}}^T cT' \left( \frac{\partial G_S}{\partial T'} + \frac{\partial M}{\partial T'} + \frac{\partial E}{\partial T'} \right) dT' - F_T - Q, \quad (6)$$


---

where  $T_{\min}$  is the lowest temperature in the domain. The first term on the right-hand side of Eq. (6) is the advective heat transport across  $I_T$ , and the integral represents the advective heat transport across  $I_S$ ,  $A$ , and  $B$ . Note also that the temperature of precipitation and river runoff are assumed to be equal to the local SST in our heat budget.

Conservation of salt can be written as

$$\frac{\partial}{\partial t} \int_0^S S' \frac{\partial V}{\partial S'} dS' = -SG_S - \int_0^S S' \left( \frac{\partial G_T}{\partial S'} + \frac{\partial M}{\partial S'} \right) dS' - F_S. \quad (7)$$

### c. Relation between the flow variables

By taking the derivative of Eq. (5) with respect to  $S$  and then multiplying with  $S$ , one obtains

$$S \frac{\partial^2 V}{\partial S \partial t} = -S \left( \frac{\partial G_T}{\partial S} + \frac{\partial G_S}{\partial S} + \frac{\partial M}{\partial S} + \frac{\partial E}{\partial S} \right). \quad (8)$$

It should be noted that the volume flows  $G_T$  and  $G_S$  represent the net transports across property surfaces that may move in space. Accordingly, it is the difference between the fluid velocity and the velocity of the property surfaces that determine these flows. Below we will show how these flows, which describe water mass transformation, are related to the non-advectional heat and salt fluxes in the interior and through the sea surface.

### b. Conservation relations

We now use the definitions introduced above to formulate conservation of volume, heat, and salt. The domain can be a basin, like the North Atlantic, or the entire ocean. In the latter case, the flow  $M$ , representing exchange with the surrounding ocean, is zero. By a straightforward extension of the  $T$ -coordinate case described in Walin (1982), the evolution of  $V(S, T, t)$  can be written as

$$\frac{\partial V}{\partial t} = -G_T - G_S - M - E. \quad (5)$$

Conservation of heat is given by

$$S \frac{\partial^2 V}{\partial S \partial t} = -G_S - S \left( \frac{\partial G_T}{\partial S} + \frac{\partial G_S}{\partial S} + \frac{\partial M}{\partial S} \right) - \frac{\partial F_S}{\partial S}. \quad (9)$$

By taking the derivative of Eq. (7) with respect to  $S$ , one obtains

$$G_S = S \left( \frac{\partial E}{\partial S} \right) - \frac{\partial F_S}{\partial S}. \quad (10)$$

The interpretation of this equation is that the water with salinity  $S$  that leaves the region by crossing the isohaline surface  $I_S$  must become more saline and that this is accomplished by evaporation (the first term) and interior diffusion (the second term). Similar manipulations using Eqs. (5) and (6) yield

$$G_T = -\frac{1}{c} \frac{\partial Q}{\partial T} - \frac{1}{c} \frac{\partial F_T}{\partial T}. \quad (11)$$

This equation means that the water with temperature  $T$  that leaves the region across the isothermal surface  $I_T$  does so as a result of heating by surface fluxes and interior diffusion.

#### *d. Relation to the one-dimensional descriptions of Walin (1977, 1982)*

It is instructive to first examine the cumulative surface fluxes as functions of either temperature or salinity. For the sake of simplicity, we here consider the entire ocean, implying that the advective exchange term  $M$  is zero. By setting  $T = T_{\max}$ , where  $T_{\max}$  is the largest temperature in the domain, we recover the description of water mass transformation in salinity coordinates from [Walin \(1977\)](#). In this case, the continuity equation for the volume in the ocean where the salinity is less than  $S$  is given by

$$\frac{\partial V(S, T_{\max}, t)}{\partial t} = -G_S(S, T_{\max}, t) - E(S, T_{\max}, t), \quad (12)$$

where  $G_S(S, T_{\max}, t)$  is the volume transport across the entire isohaline surface  $S$ . Assuming a steady state, that is,  $G_S(S, T_{\max}) + E(S, T_{\max}) = 0$ , and substituting  $G_S$  from Eq. (10), one arrives at

$$\frac{\partial SE(S, T_{\max})}{\partial S} = \frac{\partial F_S(S, T_{\max})}{\partial S}. \quad (13)$$

This implies that

$$F_S(S, T_{\max}) = SE(S, T_{\max}), \quad (14)$$

since both terms in Eq. (14) approach zero for sufficiently high or low salinities. Equation (14) shows that in a steady state the diffusive salt flux across the isohaline  $S$  is balancing the virtual salt flux  $S E(S, T_{\max})$ .

If we instead set  $S = S_{\max}$ , where  $S_{\max}$  is the largest salinity in the domain, we recover the description of water mass transformation in temperature space from [Walin \(1982\)](#). The steady state [ $G_T(S_{\max}, T) + E(S_{\max}, T) = 0$ ] heat budget for the part of the ocean where the temperature is less than  $T$  takes the form

$$\begin{aligned} F_T(S_{\max}, T) &= -Q(S_{\max}, T) \\ &+ c \int_{T_{\min}}^T E(S_{\max}, T') dT'. \end{aligned} \quad (15)$$

Thus, the diffusive heat flux across the isothermal surface  $T$  is balancing the net surface heat loss over the part of the ocean surface where the temperature is less than  $T$  ([Walin 1982](#)). Note that the integral over  $E(S_{\max}, T)$  represents the contribution to the surface heat flux due to the heat transfer associated with precipitation.

### 3. Flow representations in $S$ - $T$ space

#### *a. A continuity equation in $S$ - $T$ space*

In  $S$ - $T$  coordinates, the flows  $G_S$  and  $G_T$  transform water masses in orthogonal directions. Following [Speer \(1993\)](#), a transformation vector can be defined through

$$\mathbf{J} = \left( \frac{\partial G_S}{\partial T}, \frac{\partial G_T}{\partial S} \right). \quad (16)$$

Here,  $(\partial G_S / \partial T) dT$  gives the transformation of water toward higher salinities occurring at the salinity  $S$  in the temperature range  $T$  to  $T + dT$ , that is, the volume transport through the part of the isohaline surface  $I_S$  where the temperature is in the range  $T$  to  $T + dT$ . The term  $(\partial G_T / \partial S) dS$  gives the transformation of water toward higher temperatures in the salinity range  $S$  to  $S + dS$ , that is, the volume transport through the part of the isothermal surface  $I_T$  where the salinity is in the range  $S$  to  $S + dS$ . It is shown in [appendix C](#) that the transformation vector  $\mathbf{J}$  can also be written in terms of the net heating  $\dot{T}$  and salinization  $\dot{S}$  of the volume  $v$  as

$$\mathbf{J} = v(\dot{S}, \dot{T}), \quad (17)$$

where  $\dot{T}$  is defined through

$$v\dot{T} = \frac{\partial^2}{\partial T \partial S} \iiint_{V(S, T, t)} \frac{DT}{Dt} dV, \quad (18)$$

and  $\dot{S}$  is defined through

$$v\dot{S} = \frac{\partial^2}{\partial T \partial S} \iiint_{V(S, T, t)} \frac{DS}{Dt} dV. \quad (19)$$

By using the definition given in Eq. (4) and Eqs. (10) and (11), one can separately consider the contributions to the transformation vector from air-sea fluxes and mixing. [Speer \(1993\)](#) only included the air-sea flux contribution in his transformation vector and made an observationally based calculation for the North Atlantic.

Using the definitions from Eqs. (16) and (5), the rate of change of  $v(S, T, t)$  (the continuity equation in  $S$ - $T$  space) can be written as

$$\frac{\partial v}{\partial t} = -\nabla \cdot \mathbf{J} - \frac{\partial^2 M}{\partial T \partial S} - \frac{\partial^2 E}{\partial T \partial S}, \quad (20)$$

where  $\nabla = (\partial / \partial S, \partial / \partial T)$ . The source term related to net precipitation and runoff is usually small and can therefore often be neglected.

*b. A streamfunction describing steady-state water mass transformations*

In the following, we will consider the entire World Ocean, so that  $M$  is identical to zero. If we further assume a steady state and neglect  $E$ , Eq. (5) gives

$$0 = G_T(S, T) + G_S(S, T), \quad (21)$$

where  $G_T(S, T)$  and  $G_S(S, T)$  denote time-averaged quantities. From the definitions of Eq. (16) and (21) we obtain

$$\nabla \cdot \mathbf{J} = 0. \quad (22)$$

Alternatively, this equation can be obtained from Eq. (20). Thus, in a steady state we can define a streamfunction  $\Psi(S, T)$  as

$$\Psi(S, T) = G_T, \quad \text{or equivalently } \Psi(S, T) = -G_S. \quad (23)$$

This is the diathermohaline streamfunction of Groeskamp et al. (2014). The transformation vector can then be written as

$$\mathbf{J} = \left( -\frac{\partial \Psi}{\partial T}, \frac{\partial \Psi}{\partial S} \right). \quad (24)$$

## 4. Application

### a. Model description

The diagnostics are done using the OGCM Nucleus for European Modeling of the Ocean (NEMO) version 3.2 (Madec 2008), with the Louvain-la-Neuve Sea Ice Model, version 2 (LIM2; Fichefet and Maqueda 1997). The model is run in the ORCA1 configuration, which has a tripolar nonuniform grid with a base resolution of  $1^\circ$ . Our run is forced with the Drakkar forcing set version 4.3 (DFS4.3), which is a 40-yr European Centre for Medium-Range Weather Forecasts (ECMWF) Re-Analysis (ERA-40)-based OGCM forcing that uses radiative fluxes and monthly precipitation extracted from satellite data and has increased wind speeds compared with ERA-40. The DFS4.3 forcing has been found to reduce known biases in NEMO ORCA2<sup>3</sup> such as weak wind-driven circulation in subtropical gyres and the ACC, an unrealistic Arctic ice cover and a tropical warm bias (Brodeau et al. 2010).

The model is initiated from rest with temperature and salinity fields from the *World Ocean Atlas 2005* (WOA05; Locarnini et al. 2006; Antonov et al. 2006) and

run repeating the forcing years from 1958 to 1983 for 1500 yr. We then look at the average fluxes over the last repetition of the 26-yr forcing cycle in our analysis. After the initial spinup, the model drift is very small. All diagnostics are done online to fully resolve all temporal correlations. Our implementation of these diagnostics in the model is described in appendix A.

To account for the effects of unresolved eddies, the model uses Redi isoneutral mixing (Redi 1982) as well as parameterized eddy advection (Gent and McWilliams 1990). The isoneutral slopes used by the parameterizations are bounded by 0.01 to ensure numerical stability. They are also set to decrease linearly to zero in the top 70 m; the effect is a gradual change from isoneutral into horizontal diffusion. This dianeutral mixing that occurs due to the slope tapering in the isoneutral mixing scheme was found to induce considerable water mass transformation in the deep mixed layers in the Southern Ocean in a neutral density framework (Iudicone et al. 2008a).

Penetrative shortwave radiation, which was found to be important for water mass transformation in a neutral density framework (Iudicone et al. 2008b), is implemented in our model using a simple scheme described in Paulson and Simpson (1977). Convection is modeled as enhanced diffusion meaning that whenever  $N^2 < 10^{-12}$ , the dianeutral diffusion coefficient that is given by a turbulence closure scheme (Gaspar et al. 1990; Madec et al. 1998) is replaced by a fixed coefficient with a value of  $100 \text{ m}^2 \text{ s}^{-1}$ . We also use a tidal mixing scheme that increases the dianeutral diffusivity in the deep ocean (Simmons et al. 2004) and a diffusive bottom boundary layer parameterization that increases the diffusivity between bottom grid boxes (Beckmann and Dööscher 1997). The sea surface salinity is restored toward the WOA05 value by way of a restoring freshwater flux. The time scale of this restoration is approximately 40 days, and the restoring flux is bounded by  $4 \text{ mm day}^{-1}$ .

The zonal-mean hydrography before and after the integration is shown in Fig. 2. One notable difference between the model and observations is that the Antarctic Intermediate Water (AAIW) in the Atlantic basin does not penetrate as far north in the model hydrography as it does in nature. However, the water mass properties of our model generally have a good qualitative agreement with the observed hydrography.

Figure 3 shows the diathermohaline streamfunction. The amplitudes of the streamfunction cells owing to the advective part, that is, the thermohaline streamfunction, compares well to estimates from earlier studies with NEMO at higher resolution. The amplitude of the tropical cell is about 25 Sverdrups ( $\text{Sv}; 1 \text{ Sv} \equiv 10^6 \text{ m}^3 \text{ s}^{-1}$ ), which is the same as Döös et al. (2012) found in their  $1/4^\circ$  NEMO run, but considerably larger than the value of 8 Sv

<sup>3</sup> ORCA2 uses a tripolar nonuniform grid with a base resolution of  $2^\circ$ .

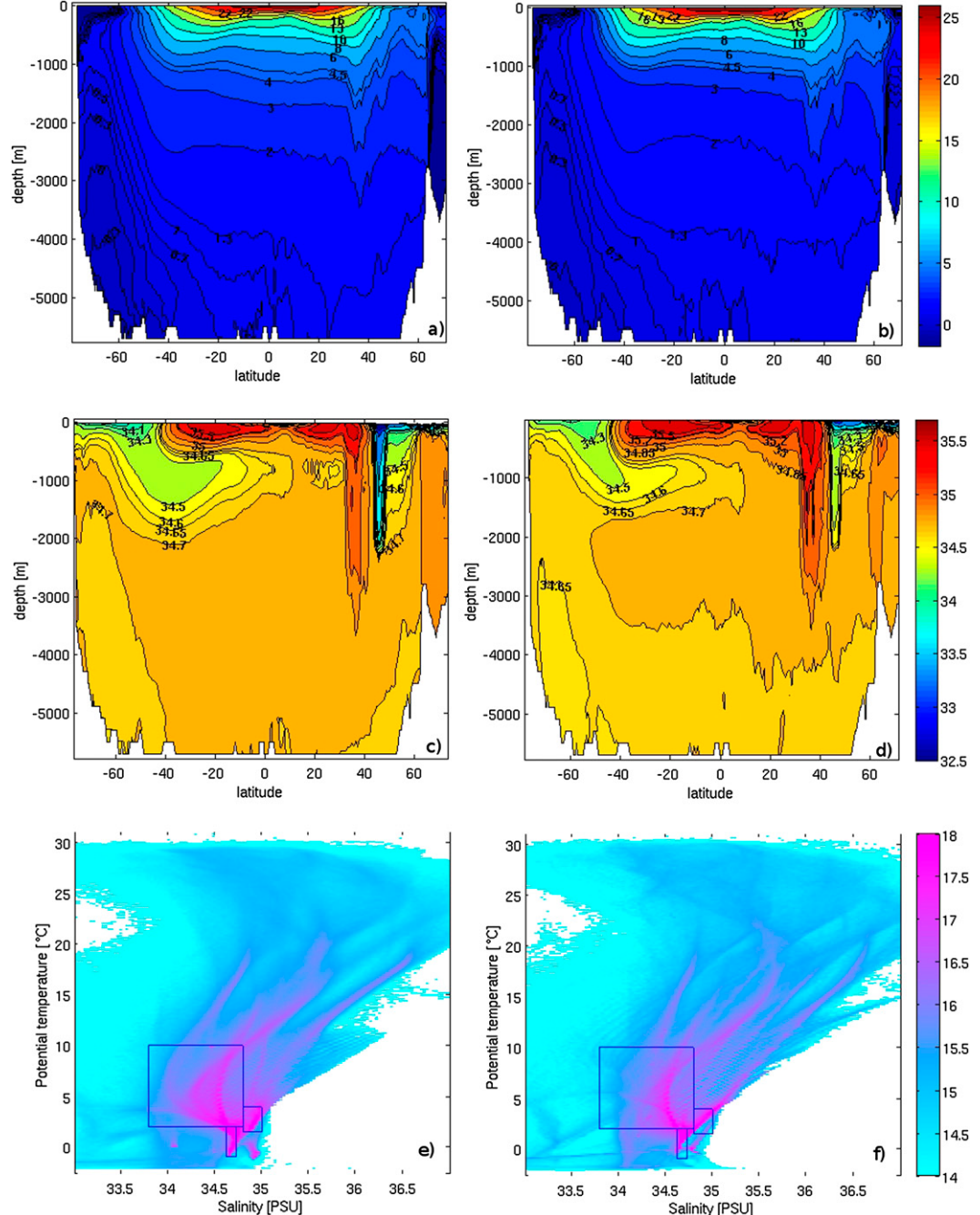


FIG. 2. Initial and final ocean states. (a) Zonal-mean potential temperature ( $^{\circ}$ C) in WOA05, (b) zonal-mean potential temperature after the integration, (c) zonal-mean salinity (psu) in WOA05, (d) zonal-mean salinity after the integration, (e)  $\log_{10}v(S, T)$  [ $m^3(psu \ ^{\circ}C)^{-1}$ ] calculated from WOA05, and (f)  $\log_{10}v(S, T)$  after the integration. The large box in (e) and (f) contains AAIW, the box to its right contains NADW, and the box below it contains AABW + CDW.

found by [Zika et al. \(2012\)](#) for the tropical cell in the University of Victoria Climate Model at a  $1.8^{\circ}$  latitude by  $3.6^{\circ}$  longitude resolution. The amplitude of the conveyor belt cell in the present run is about  $29\text{ Sv}$ , which is slightly less than the  $32\text{ Sv}$  found by [Döös et al. \(2012\)](#) and again considerably larger than the  $15\text{ Sv}$  found by [Zika et al. \(2012\)](#).

The volume distribution function  $v(S, T)$  before and after the integration is shown in [Figs. 2f and 2e](#), with some major water masses indicated by squares. The water mass definitions are taken from [Emery and Meincke \(1986\)](#). The large square shows AAIW, which is defined by  $S \in [33.8, 34.8]$  psu and  $T \in [2, 10] \ ^{\circ}\text{C}$ . The colder of the

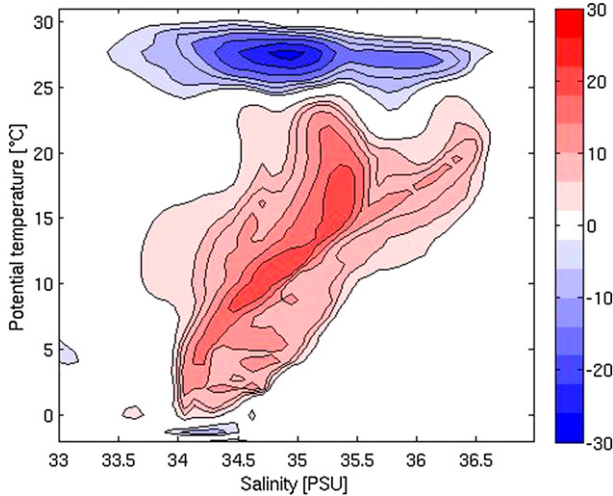


FIG. 3. The diathermohaline streamfunction  $\Psi(S, T)$  [ $\text{Sv}$  ( $10^6 \text{ m}^3 \text{s}^{-1}$ )]. The advective part is computed online using the method described in Döös et al. (2012), and the local part is computed from monthly means following Groeskamp et al. (2014). The streamfunction is dominated by the advective contribution, with the notable exception that the anticyclonic (blue) cell occurring in subzero temperatures approximately between salinities of 34 and 34.5 psu is almost completely due to the local part. The streamfunction is based on the sum of the resolved model velocity and the parameterized eddy advection due to the Gent and McWilliams (1990) scheme.

smaller boxes shows Antarctic Bottom Water (AABW) + Circumpolar Deep Water (CDW) (they are added together because their  $S$ - $T$  definitions overlap) defined by  $S \in [34.62, 34.73]$  psu and  $T \in [-0.9, 2]$  °C. Finally, the warmer of the small boxes shows North Atlantic Deep Water (NADW), which is defined by  $S \in [34.8, 35]$  psu and  $T \in [1.5, 4]$  °C. There are some notable differences in the two volume distribution functions. For example, there is a clear change in the  $S$ - $T$  geometry of the local peak in the volume distribution function found to the right of the AABW + CDW box. This peak corresponds to the deep water in the Arctic basin, and it has clearly changed so that the density difference within the water mass is smaller after the integration, possibly a result of strong isoneutral diffusion.

#### b. Distribution of surface and interior fluxes

We have computed the surface flux functions  $Q(S, T, t)$  and  $E(S, T, t)$  as well as their interior counterparts  $F_S(S, T, t)$  and  $F_T(S, T, t)$  from our steady state NEMO run and will here discuss their time-mean features. We have also split the interior flux functions into separate contributions for different physical processes. That is, we have separate  $F_T$  functions for isoneutral diffusion, dianeutral diffusion, convection, and the bottom boundary layer parameterization. The flux function  $Q(S, T)$  also incorporates the penetrating part of the

shortwave radiation. The salinity fluxes  $F_S$  are treated in a similar fashion. The domain is the global ocean, so that  $M$  is zero.

**Figure 4** shows the surface heat and salinity forcings  $Q(S_{\max}, T)$  and  $SE(S, T_{\max})$  from the model simulation and the interior fluxes  $F_T(S_{\max}, T)$  and  $F_S(S, T_{\max})$  process by process. Note that the integral over  $E(S_{\max}, T)$  in Eq. (15) that represents the contribution to the surface heat flux due to the heat transfer associated with precipitation is added to the term labeled  $Q(S_{\max}, T)$  in Fig. 4. The sign convention used is that a positive  $F_T(S_{\max}, T)$  [ $F_S(S, T_{\max})$ ] means a flux toward increasing temperature (salinity), and the surface fluxes are positive when they are upward. The surface fluxes warm the ocean at temperatures greater than 22°C and cool the ocean at lower temperatures. Thus, the surface heat flux acts to increase the temperature range of the ocean. This is mainly balanced by dianeutral diffusion, although isoneutral diffusion is also important. Isoneutral diffusion is in fact the most important heat source for the water that is colder than 5°C. The boundary layer parameterization as well as convection have negligible effects on these heat and salinity budgets and have therefore been excluded from Fig. 4. The virtual salt flux associated with the cumulative surface freshwater flux acts to freshen the ocean at salinities lower than about 34.8 psu and increase the salinity of the water with  $S > 34.8$  psu. This is balanced by a diffusive cross-isohaline flux from high toward low salinity; dianeutral and isoneutral diffusion contribute almost equally to this flux. The residual heat flux is very small compared to the important terms in the heat budget. The residual salinity flux is larger, but still much smaller than the dominant terms in the salinity budget.

**Figures 4b and 4d** show the contributions from the most important processes to  $G_T(S_{\max}, T)$  and  $G_S(S, T_{\max})$  [that is  $G_T$  and  $G_S$  in the traditional one-dimensional water mass transformation framework described in Walin (1977, 1982)]. The terms  $G_T(S_{\max}, T)$  and  $G_S(S, T_{\max})$  should thus equal the sum of the curves shown in Figs. 4b and 4d, except for small contributions from the neglected convection and bottom boundary layer terms. The model drift is small so  $G_T(S_{\max}, T)$  and  $G_S(S, T_{\max})$  should roughly equal  $E(S_{\max}, T)$  and  $E(S, T_{\max})$ , where the  $E$  terms are of the order of 2 Sv, which is comparable to the net equatorward oceanic freshwater transport into the tropics (e.g., Wijffels et al. 1992; Nilsson and Körnich 2008). There are, however, residuals in both the temperature and salinity case. The residuals are typically much smaller than the contributions to  $G_T(S_{\max}, T)$  and  $G_S(S, T_{\max})$  from isoneutral diffusion, dianeutral diffusion, and surface fluxes, but much larger than the respective  $\partial V / \partial t$  terms of each budget. This means that the

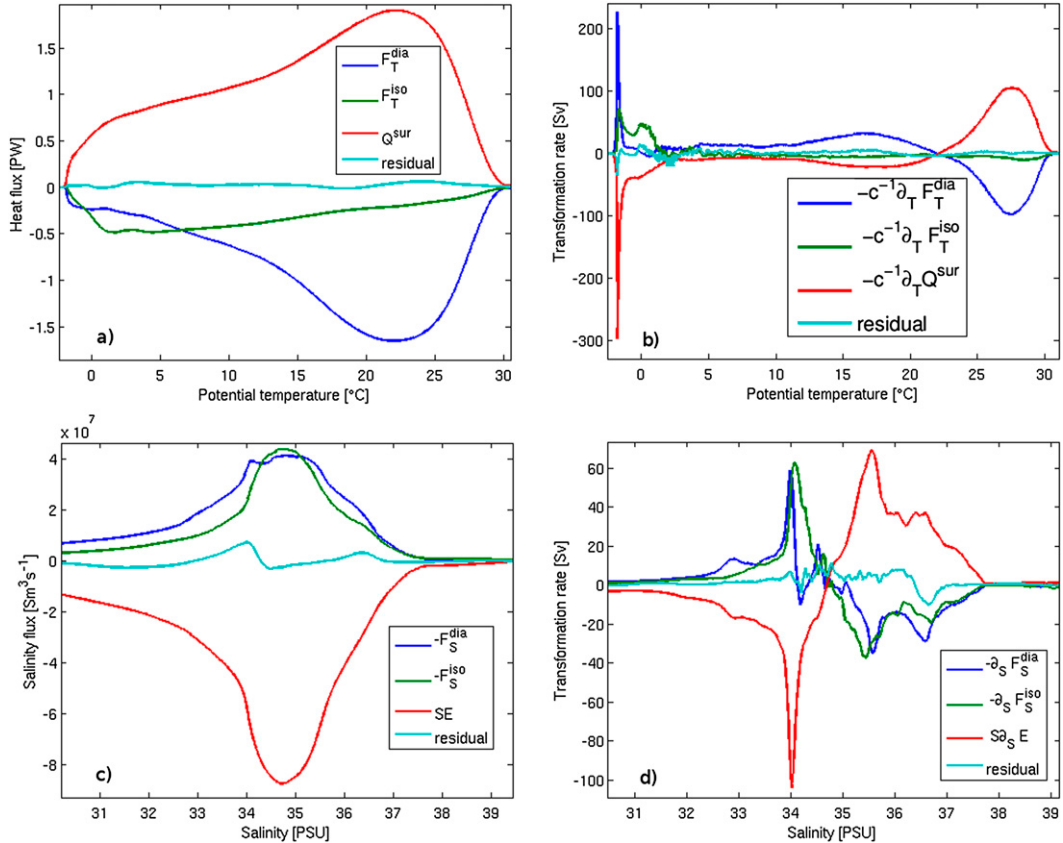


FIG. 4. Water mass transformation in  $S$  and  $T$  space. (a) The cumulative fluxes  $Q(S_{\max}, T)$  and  $F_T(S_{\max}, T)$ , and (b)  $c^{-1}\partial Q/\partial T(S_{\max}, T)$  and  $c^{-1}\partial F_T/\partial T(S_{\max}, T)$ . (c) The cumulative fluxes  $SE(S, T_{\max})$  and  $F_S(S, T_{\max})$ , and (d)  $S\partial E/\partial S(S, T_{\max})$  and  $\partial F_S/\partial S(S, T_{\max})$ . All panels also show the residual of the calculation. The superscript dia (iso) is given to fluxes due to dianeutral (isoneutral) diffusion.

transformation framework, at least in the current implementation, is well suited to look at the effects of the different physical processes on water mass transformation, but not quite accurate enough to close a volume budget or to build a streamfunction.

Positive values in Figs. 4b and 4d indicate transformations toward warmer or saltier water. Figure 4b shows that in the water that is warmer than about  $5^{\circ}\text{C}$ , we have an approximate balance between the transformations due to dianeutral diffusion and surface fluxes, but in the colder waters isoneutral diffusion is also important. There is also a pronounced transformation peak around the freezing point that is associated with sea ice formation. Here, the main balance is between transformation toward colder water masses by surface heat loss and transformation toward warmer water masses due to dianeutral diffusion. A similar peak is not identifiable in salinity coordinates, which indicates that the transformations associated with sea ice formation occur over a wider range of salinities than temperatures.

The net surface flux of freshwater transforms the waters with salinities above about 34.8 psu toward higher salinities and fresher waters toward lower salinities. Thus, the net surface freshwater flux acts to increase the salinity range in the ocean. Dianeutral and isoneutral diffusive fluxes are about equally efficient in decreasing the salinity range.

### c. Transformations in $S$ - $T$ space

In this section, we present the transformation vector  $\mathbf{J}$  from our NEMO run. In terms of our flux functions  $\mathbf{J}$  is defined according to

$$\mathbf{J} = \left( S \frac{\partial^2 E}{\partial T \partial S} - \frac{\partial^2 F_S}{\partial T \partial S}, -\frac{1}{c} \frac{\partial^2 Q}{\partial T \partial S} - \frac{1}{c} \frac{\partial^2 F_T}{\partial T \partial S} \right). \quad (25)$$

Figure 5 shows the transformation vector plotted on top of the logarithm of the volume distribution function  $v$ . The red contours show water types that exist only in the Atlantic Ocean, defined as the ocean in the Atlantic

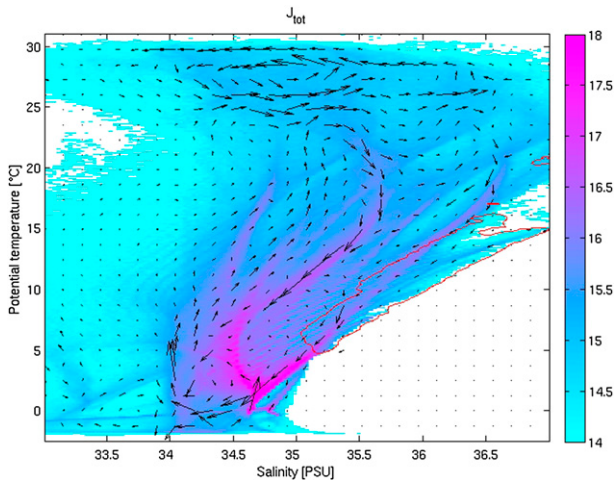


FIG. 5. The total transformation vector  $\mathbf{J}$  from all processes plotted on top of the logarithm value of the volume distribution function  $\{\log_{10}(v) [\text{m}^3(\text{psu } ^\circ\text{C})^{-1}]\}$ . The red contours show water types that only exist in the Atlantic Ocean, defined as the ocean in the Atlantic sector north of latitude 50°S and south of the Arctic Ocean.

sectors north of latitude 50°S and south of the Arctic Ocean. The transformation vector shows two distinct circulation cells, similar to the two stronger ones depicted by the diathermal streamfunction shown in Fig. 3. One warm anticyclonic cell occupies the temperature range above 25°C, and the salinity range between approximately 33.5 and 35.5 psu. This cell was called the tropical cell by Döös et al. (2012). There is also a weaker branch of this cell in the same temperature range, but in the salinity range between 35.5 and 36.5 psu. A large cyclonic cell is present in the waters that are colder than 25°C. Döös et al. (2012) dubbed this cell the conveyor belt cell, because it is related to interocean exchange. The diathermal streamfunction also shows a cold anticyclonic cell occurring in temperatures below zero and salinities between 34 and 34.5 psu; however, this cell is not recognizable in the vector field in Fig. 5.

Figure 6 shows the contribution to  $\mathbf{J}$  from the most important processes:  $\mathbf{J}_{\text{sur}}$  is the contribution from surface fluxes, including the penetrative part of the shortwave radiation [this vector is plotted on top of the surface area distribution function, which is defined below in Eq. (26)],  $\mathbf{J}_{\text{int}}$  is the contribution from all internal processes,  $\mathbf{J}_{\text{dia}}$  is the contribution from dianutral diffusion, and  $\mathbf{J}_{\text{iso}}$  is the contribution from isoneutral diffusion. The lengths of the arrows in the different panels are scaled against a common measure so that all panels are directly comparable. The contributions from convection and the diffusive bottom boundary layer scheme have been left out because they are small everywhere, so

that  $\mathbf{J}_{\text{int}} \approx \mathbf{J}_{\text{iso}} + \mathbf{J}_{\text{dia}}$ . It should be noted that the convection is generally a dominating component of the vertical fluxes of heat and salt in the near-surface mixed layer (see, e.g., Hieronymus and Nycander 2013a,b). However, the convective fluxes, although large in magnitude, are vertical and hence essentially parallel to the isothermal and isohaline surfaces within the mixed layer. Thus, only a tiny fraction of the convective fluxes crosses the nearly vertical isohaline and isothermal surfaces in the mixed layer and hence yield a negligible water mass transformation.

Contrary to earlier ideas that a significant proportion of the water mass transformations occurred in the interior ocean (Munk 1966), recent analyses and data suggest that the bulk of the water mass transformation occurs near the sea surface (Marshall and Speer 2012; Marshall et al. 1999). Therefore, it is interesting to examine how the area at the ocean surface is distributed in  $S$ - $T$  space. For this purpose, we introduce a surface area distribution function  $a(S, T)$ , defined as

$$a(S, T) = \frac{\partial^2 A}{\partial T \partial S}. \quad (26)$$

The function  $a(S, T)$  is often more closely linked to areas of strong transformation than the function  $v(S, T)$ . This can be seen in Fig. 6a, where  $\mathbf{J}_{\text{sur}}$  is plotted on top of  $a$ . The structure of the function  $a$  is different from that of the function  $v$  in that high values are found mostly along a central branch in the case of  $a$ , whereas high values of  $v$  are distributed along several different branches. The peak values of  $a$  and  $v$  are also disjoint in  $S$ - $T$  space: a large part of the volume exists in a range  $S > 34.5$  psu and  $T \in [0, 5]^\circ\text{C}$ , where there is very little area exposed to the surface. The transformation of water into that range is therefore only weakly affected by surface fluxes; instead it is the transformation due to isoneutral diffusion that connects the area of large  $a$  values around the freezing point to the aforementioned range of large  $v$  values, as seen in Fig. 6c. Judging from the  $S$ - $T$  range where this transformation occurs, it is most likely due to strong isoneutral fluxes between waters of Atlantic and Antarctic origin that meet in the Southern Ocean.

Another feature, which was also pointed out by Speer (1993), is that the surface fluxes tend to transform the water outward in  $S$ - $T$  space. The surface fluxes thus create the extreme values of  $S$  and  $T$  in the distribution, and the internal processes, that is, mixing, act to reduce those extreme values. Figure 6 also shows some important features of the water mass transformations that are missed when viewed in only  $T$  or  $S$  space. For example, Fig. 6a shows that surface fluxes transform the water with temperature and salinity around 5°C and

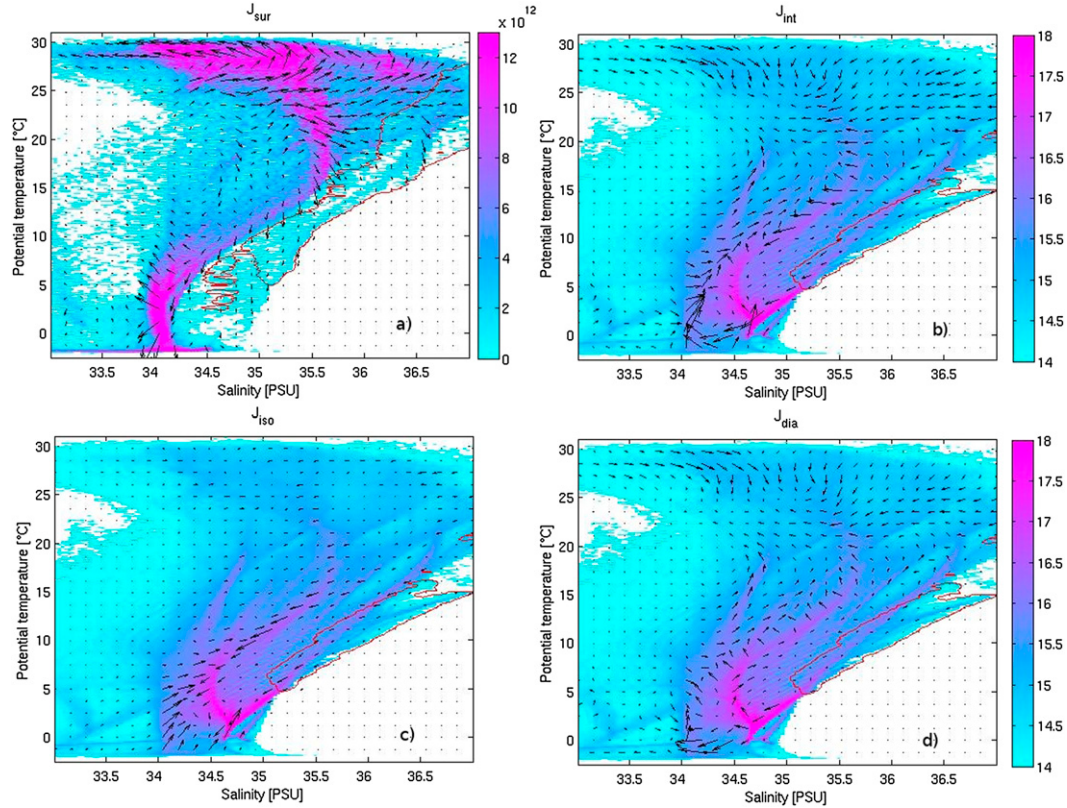


FIG. 6. The transformation vector  $\mathbf{J}$  for various processes. The surface transformation vector is plotted on top of the surface area distribution function  $a$  [ $\text{m}^2(\text{psu} \text{ } ^\circ\text{C})^{-1}$ ], and the others are plotted on top of the logarithm value of the volume distribution function  $v$   $\{\log_{10}(v)$  [ $\text{m}^3(\text{psu} \text{ } ^\circ\text{C})^{-1}$ ]\}. The red contours show water types that only exist in the Atlantic Ocean, defined as the ocean in the Atlantic sectors north of latitude 50°S and south of the Arctic Ocean. The term  $\mathbf{J}_{\text{sur}}$  is the contribution to  $\mathbf{J}$  from surface fluxes including the penetrative part of the shortwave radiation,  $\mathbf{J}_{\text{int}}$  is the contribution from all internal processes,  $\mathbf{J}_{\text{dia}}$  is the contribution from dianeutral diffusion, and  $\mathbf{J}_{\text{iso}}$  is the contribution from isoneutral diffusion.

34.1 psu toward higher temperatures, while Fig. 4b only shows that the net surface transformation in that temperature range is toward lower temperatures. Likewise for salinities higher than about 34.8 psu, Fig. 4d shows that the net surface transformation is toward higher salinities. However, Fig. 6a shows that for high temperatures the transformation is in fact the opposite.

By comparing the process-by-process transformation vectors in Fig. 6 with the net transformation vectors in Fig. 5, we can get a general view of what processes are responsible for the transformations in specific  $S$ - $T$  regions and also to some extent in which ocean basin they occur. For example, focusing on the warm anticlockwise, or tropical, cell in Fig. 6, we can see that these transformations result from surface fluxes and dianeutral diffusion. The negligible role of isoneutral fluxes for this cell is expected, since those fluxes typically are rather weak at low latitudes (Ferrari and Ferreira 2011; Hieronymus and Nycander 2013a). The tropical cell occurs mainly near the surface: the penetrative shortwave radiation

reaches perhaps 100 m, and  $\mathbf{J}_{\text{dia}}$  calculated below 100 m (Fig. 7b) shows no strong transformation in this  $S$ - $T$  range, implying that it is confined to the upper 100 m. Further, the main branch of the tropical cell is situated on top of a peak in the area distribution function, and there is a secondary weaker branch in the more saline waters, which is situated on top of a different peak in the area distribution function. The peak under the main branch corresponds to waters in the tropical Pacific, and the peak under the weaker, more saline, branch corresponds to waters in the tropical Atlantic.

Döös et al. (2012) provided a simple four-segment description of the tropical cell in real space. The first segment in  $S$ - $T$  space starts in the top-left corner of the cell. This segment represents water flowing poleward from the warm pool, while becoming cooler and more saline. This cooling and salinization is, as can be seen from Fig. 6d, the result of dianeutral diffusion. The second segment in their description is where the water in the tropical cell reaches its minimum temperature.

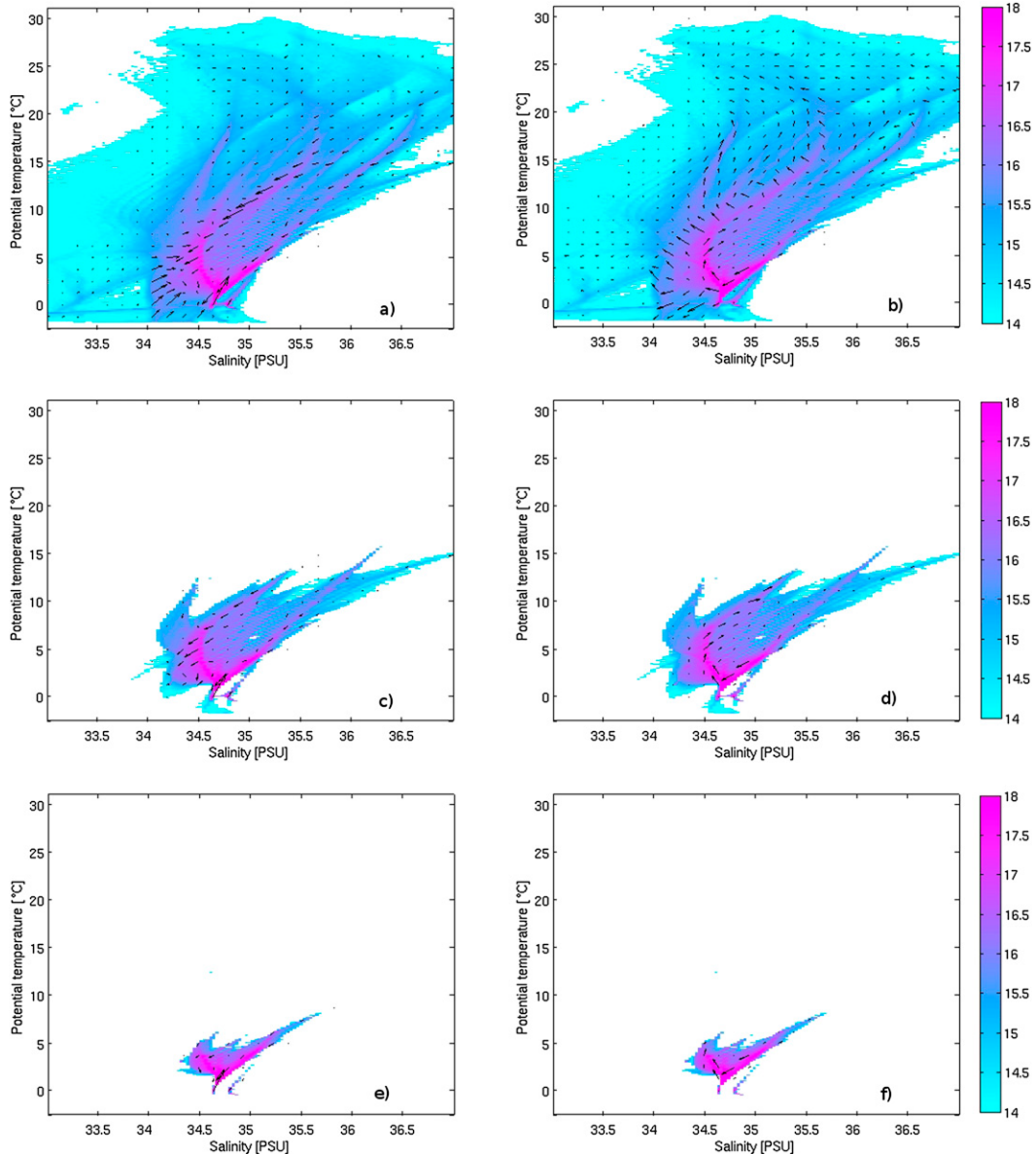


FIG. 7. (left)  $\mathbf{J}_{\text{iso}}$  and (right)  $\mathbf{J}_{\text{dia}}$ . (a), (b) Based on the diffusive fluxes that occur below 100 m, (c), (d) based on those below 500 m, and (e), (f) based on those below 1000 m. All are plotted on top of the logarithm value of the volume distribution function  $v \{\log_{10}(v) [\text{m}^3(\text{psu } ^\circ\text{C})^{-1}]\}$  and scaled so that the arrow lengths are directly comparable to those in Figs. 5 and 6.

Here, the water is subducted into the thermocline of the equator and flows equatorward and joins the eastward-flowing equatorial undercurrent. The second segment is thought to be adiabatic to the first order and result in very little water mass transformation; it is thus more or less a point in  $S-T$  space. The third segment represents westward flow of water originating from the cold pool. The net evaporation and strong heat flux into the ocean in the eastern equatorial Pacific results in transformations toward warmer and saltier waters. The final

segment in this description starts in the top-right corner of the tropical cell. This segment involves westward-flowing water in the warm pool, which is freshened by net precipitation. Originally, it was thought that this freshening occurred at a nearly constant temperature because of relatively weak surface heat fluxes. However, Figs. 6a and 6d show that the temperature is in fact kept nearly constant because the warming due to surface fluxes is nearly balanced by the cooling due to dianeutral diffusion.

The large clockwise (“conveyor belt”) cell in Fig. 5 is in contrast to the tropical cell also largely driven by isoneutral diffusion, which can be seen in Fig. 6c. Both cells, however, appear to have distinct Pacific and Atlantic branches. The warmest water in the conveyor belt cell has a temperature of about 25°C and is highly saline. The transformation of these warm and saline waters into colder and fresher waters can be divided into two branches. The first one is initiated by cooling surface fluxes when the salinity reaches about 35.5 psu and happens mainly in the Indo-Pacific Ocean. The second branch is altogether situated in the Atlantic Ocean. It is also initiated by cooling surface fluxes; however, the starting point is found for salinities of about 36.5 psu. Further transformations into colder water are achieved by isoneutral diffusion and surface fluxes in both branches. Zika et al. (2013) studied a streamfunction in temperature–depth coordinates and found three overturning cells: a shallow cell coincident with the subtropical gyres, a deep cell coincident with the upper limb of the meridional overturning circulation, and a bottom cell coincident with AABW. They also projected these cells into  $S$ – $T$  coordinates, and found that the shallow and deep cell together made up what we call the conveyor belt cell. The conveyor belt cell that we observe in  $S$ – $T$  coordinates thus reflect transformations that occur both in the subtropical gyres and in the ocean volume occupied by deep and intermediate water masses such as, for example, NADW and AAIW.

Ferrari and Ferreira (2011) found that the strength of the abyssal mixing has a profound effect on the strength of the meridional overturning circulation, in contrast to the oceanic heat transport, which they found to be highly surface intensified and hence relatively insensitive to the strength of the abyssal mixing. The strength of the abyssal mixing also influences the water mass transformation in  $S$ – $T$  space. However, the  $S$ – $T$  range that occurs in the deep ocean is much smaller than that in the upper ocean, so the effect of abyssal mixing is only important in a very narrow  $S$ – $T$  range. Figure 7 shows the transformation that occurs below a few selected surfaces of constant depth. It is especially clear from the right column, which shows  $\mathbf{J}_{\text{dia}}$ , that the transformation in the narrow  $S$ – $T$  range that exists at 1000 m is dominated by transformations that occur below that depth. The strength of this deep transformation appears to depend on the tidal mixing parameterization, as we have found this transformation to be weaker in shorter runs without the parameterization. The maximum values of  $G_T(S_{\max}, T)$  and  $G_S(S, T_{\max})$  calculated below the constant depth surfaces are given in Table 1.

TABLE 1. Maximum values of  $G_T^{\text{dia}}(S_{\max}, T)$ ,  $G_T^{\text{iso}}(S_{\max}, T)$ ,  $G_S^{\text{dia}}(S, T_{\max})$ , and  $G_S^{\text{iso}}(S, T_{\max})$  calculated below 100, 500, and 1000 m. A positive  $G_T$  ( $G_S$ ) value indicates a transformation toward higher temperatures (salinities). Transports are given in Sverdrups.

Depth	100	500	1000
$G_T^{\text{dia}}(S_{\max}, T)$	43	14	14
$G_T^{\text{iso}}(S_{\max}, T)$	42	-30	-21
$G_S^{\text{dia}}(S, T_{\max})$	-37	20	-7
$G_S^{\text{iso}}(S, T_{\max})$	46	-19	-12

#### d. Formation

Figure 8a shows the divergence of the transformation vector  $\mathbf{J}_{\text{sur}}$ , and Fig. 8b shows the divergence of the transformation vector  $\mathbf{J}_{\text{int}}$ . From those figures it is readily seen how the formation ( $\nabla \cdot \mathbf{J}_{\text{sur}} < 0$ ) and destruction ( $\nabla \cdot \mathbf{J}_{\text{sur}} > 0$ ) of water masses due to surface fluxes are balanced by destruction and formation due to internal mixing processes.

In a sense one could argue that the different water masses are formed by surface fluxes and destroyed by internal mixing, since the surface fluxes create the extreme values of  $T$  and  $S$  in the ocean. However, the typical  $S$ – $T$  characteristics of the large deep-water masses in the ocean are not the same as the  $S$ – $T$  characteristics of the surface water that convects at high latitudes to form these water masses. This is because of a significant mixing with ambient waters, for example, through entrainment into dense overflow currents [the formation of NADW through mixing of its different source waters is discussed by Swift (1984)]. As a result,  $\mathbf{J}_{\text{sur}}$  is not typically convergent in the  $S$ – $T$  range around NADW (approximately  $T \in [1.5, 4]^\circ\text{C}$  and  $S \in [34.8, 35]$  psu; Emery and Meincke 1986), but rather in a range that is colder and less saline than that occupied by NADW.

The divergence fields are rather spiky and have therefore been filtered to improve the visualization. This spikiness is owing to the fact that a vast majority of the water volume occupies a very narrow  $S$ – $T$  interval. In a steady state,  $\nabla \cdot \mathbf{J}_{\text{sur}} + \nabla \cdot \mathbf{J}_{\text{int}}$  should equal the negligible contribution from the freshwater term,  $e = \partial^2 E / (\partial S \partial T)$ , to the volume budget as seen from Eq. (20). However, in our case a total agreement is not expected because of model drift, discretization errors, and numerical mixing. Numerical mixing has been found to have a large impact on the tracer fields in many different types of ocean models (Maqueda and Holloway 2006; Burchard and Rennau 2008). The difficulty with this analysis is to match tendencies in temperature and salinity to trends in volume for water masses with different salinities and temperatures. Closing just the heat or salt budget can be done very accurately (see, e.g., Hieronymus and Nylander 2013a).

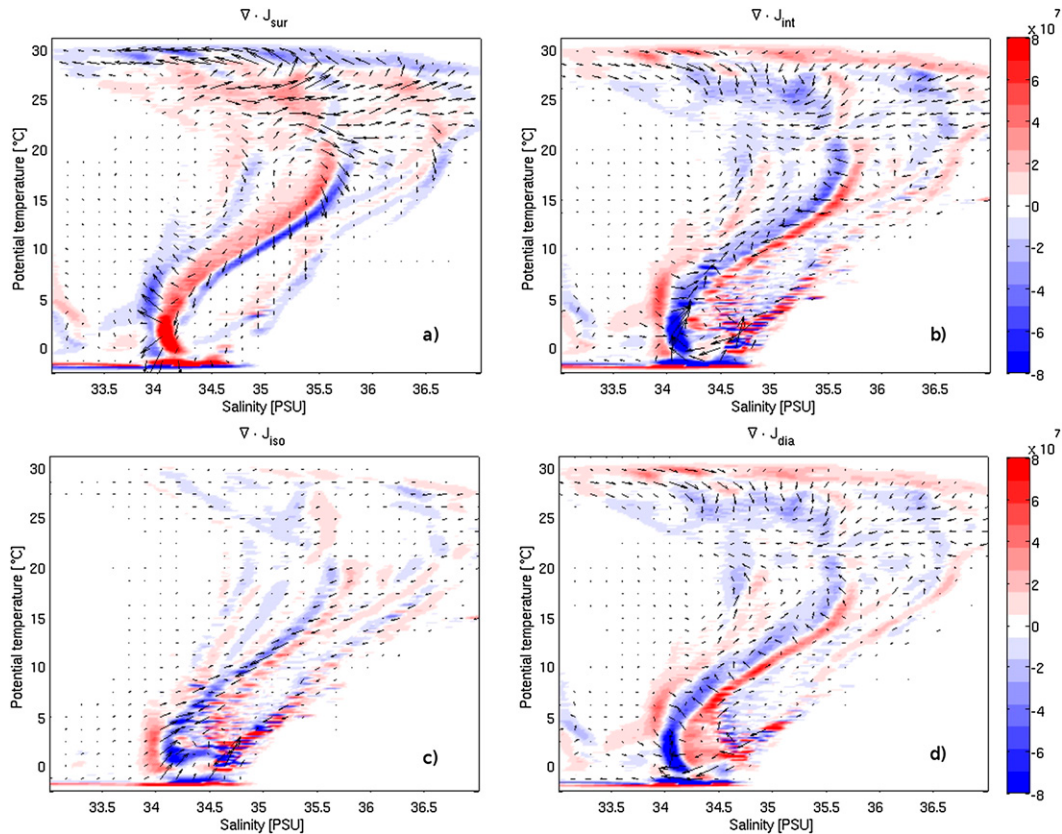


FIG. 8. The transformation vector  $\mathbf{J}$  and its divergence: the (a)  $\mathbf{J}_{\text{sur}}$ , (b)  $\mathbf{J}_{\text{int}}$ , (c)  $\mathbf{J}_{\text{iso}}$ , and (d)  $\mathbf{J}_{\text{dia}}$ . The  $S$ - $T$  divergence is given in units of  $\text{m}^3(\text{psu } ^\circ\text{C s})^{-1}$ .

[Figure 8a](#) shows that the warmest water is created by surface fluxes, and [Fig. 8d](#) shows that it is destroyed primarily by dianeutral diffusion. The water masses with temperatures between 20° and 28°C are mostly formed by dianeutral diffusion and destroyed by surface fluxes. There is an extended central band of water mass destruction due to surface fluxes that stretches from temperatures of about  $-0.5^\circ\text{C}$  and salinities between about 34 and 34.3 psu to temperatures of about 20°C and salinities between 35.4 and 35.7 psu. The location of this band of water mass destruction approximately coincides with the location of the central peak in the surface area distribution function  $a(S, T)$  (see [Fig. 6](#)). Thus, air-sea fluxes act to transform water masses away from this  $S$ - $T$  range that covers a relatively large area of the sea surface.

Just as in the temperature-only case, shown in [Fig. 4](#), there is strong formation and destruction around the freezing point, where the coldest water is formed by surface fluxes and destroyed by isoneutral and dianeutral diffusion. Sea ice formation is obviously an important process in this  $S$ - $T$  region.

There is also an interesting region located in  $S$ - $T$  space at salinities between roughly 34.2 and 34.7 psu and

temperatures between about 0° and 2°C, where the main balance is between formation due to isoneutral fluxes and destruction due to dianeutral fluxes, as seen in [Figs. 8c,d](#) and [9c,d](#). This region is primarily occupied by the deep-water masses in the model, and it is an interesting feature that those deep-water masses tend to be created by isoneutral diffusion. [Hieronymus and Nycander \(2013a\)](#) found that the downward heat flux from dianeutral diffusion was nearly balanced by an upward heat flux from isoneutral diffusion in a calculation of the heat budget in a similar setup of the NEMO model. It appears that the water mass transformation induced by isoneutral diffusion in a similar way balances that induced by dianeutral diffusion in the temperature region around 2°C in [Fig. 4](#).

The middepth salinity minimum associated with AAIW occurs, in this model, at approximately  $T \in [0, 4]^\circ\text{C}$  and  $S \in [34, 34.5]$  psu.<sup>4</sup> In [Fig. 9](#), which shows

<sup>4</sup>This is not clearly seen from the zonal-mean transects in [Fig. 2](#), so the  $S$ - $T$  values are determined from transects with no zonal averaging.

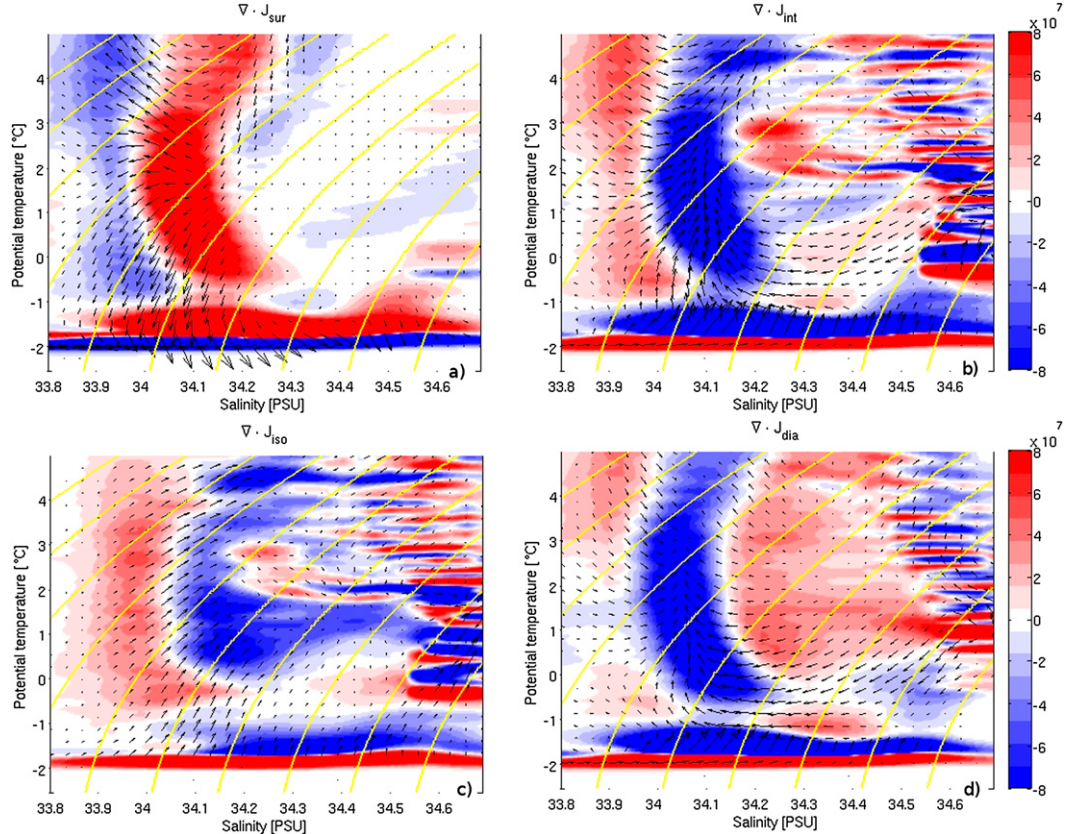


FIG. 9. A closeup of the vector  $\mathbf{J}$ , and its divergence: (a)  $\mathbf{J}_{\text{sur}}$ , (b)  $\mathbf{J}_{\text{int}}$ , (c)  $\mathbf{J}_{\text{iso}}$ , and (d)  $\mathbf{J}_{\text{dia}}$ . The yellow lines are level curves of surface-referenced potential density. Note that the curvature of those lines differs significantly for different reference pressures and that flow along these lines are hence not necessarily flowing in a neutral direction. The  $S-T$  divergence is given in units of  $\text{m}^3(\text{psu } ^\circ\text{C s})^{-1}$ .

a closeup of the transformation vector  $\mathbf{J}$  and its divergence, we can see that surface fluxes create a possible source water for AAIW at salinities that are slightly lower than those that characterize the model's AAIW and act mostly to destroy the water in the AAIW range. Both the dianeutral and the isoneutral diffusive fluxes meanwhile show a net production. Destruction of AAIW by surface fluxes was also found by Iudicone et al. (2008a). There is also a hint of a possible separation between equatorward- and poleward-flowing waters seen in the transformation vector due to surface fluxes at salinities around 34.1 psu. The water that is warmer than  $2^\circ\text{C}$  at that salinity is further warmed, and the water that is colder than  $2^\circ\text{C}$  is further cooled, which seems to indicate that the cooling branch is flowing poleward and the warming branch is flowing equatorward.

#### e. Projection into geographical space

The sea surface temperature and salinity fields  $T_S(x, y, t)$  and  $S_S(x, y, t)$  can be used to project the water mass formation due to the surface fluxes  $\nabla \cdot \mathbf{J}_{\text{sur}}(S, T, t)$  into

geographical space. Formally, a projected water mass formation can be defined by

$$\mathcal{F}(x, y, t) = \frac{\nabla \cdot \mathbf{J}_{\text{sur}}[S_S(x, y, t), T_S(x, y, t), t]}{a[S_S(x, y, t), T_S(x, y, t), t]}. \quad (27)$$

Note that  $\mathcal{F}(x, y, t)$ , having the units meters per second, satisfies

$$\iint_{A(S, T, t)} \mathcal{F} dA = \int^S \int^T \nabla \cdot \mathbf{J}_{\text{sur}} dS dT.$$

Figure 10 shows the geographically mapped water mass formation  $\mathcal{F}$  calculated using monthly averaged data for August and February. The penetrative part of the shortwave radiation is not a surface flux and is therefore not included in  $\mathcal{F}(x, y, t)$ . Before discussing the results of Fig. 10, we note that Brambilla et al. (2008) used the same projection technique to generate formation maps in geographical coordinates for some specific water types. Both Brambilla et al. (2008) and Maze et al. (2009) have calculated formation maps for selected

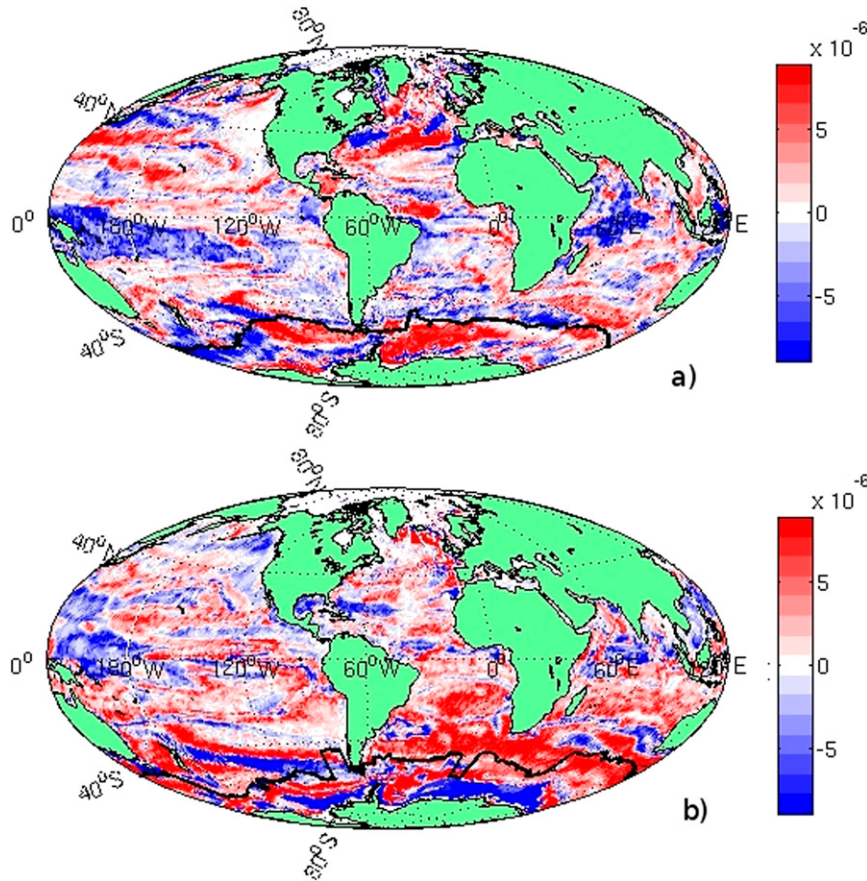


FIG. 10. Water mass formation projected from  $S\text{-}T$  coordinates into geographical coordinates.  
 (a) February values of  $\mathcal{F}(x, y, t)$  and (b) August values of  $\mathcal{F}(x, y, t)$  (both  $\text{m s}^{-1}$ ).

water types; that is, they have projected the formation within a certain density or temperature class to the geographical distribution of the sea surface density or temperature. This procedure yields one map for each water mass class. In contrast, Fig. 10 illustrates the net formation as a function of spatial location. The main limitation with this projection is that  $\nabla \cdot \mathbf{J}_{\text{sur}}(S, T, t)$  is the sum of contributions from all points in geographical space that have the same  $T$  and  $S$  values at the sea surface. Thus, all locations in geographical space with the same  $T$  and  $S$  values will have the same projected net formation  $\mathcal{F}(x, y, t)$  regardless of what the local formation in geographical space may be.

Figure 11 shows the different thermal and haline forcings that drive the water mass transformation. They have all been projected from  $S\text{-}T$  coordinates into geographical coordinates, using the same technique that was used to project the water mass formation. The projected monthly averaged heat and freshwater fluxes are similar, but not identical, to monthly averaged heat and freshwater fluxes calculated directly in geographical coordinates. However, the projected fluxes are more

readily usable to explain different aspects of Fig. 10, since they are produced in the same way following water masses. Figures 11a and 11b show the net freshwater flux from evaporation, precipitation, and runoff in units of meters per second, Figs. 11c and 11d show the net “freshwater flux” (the salt flux from brine release and ice melt is converted into a freshwater flux to ease comparison) from ice formation and melt in units of meters per second, and finally, Figs. 11e and 11f show the net heat flux in units of watts per square meter. Figure 12 shows monthly averages of  $\nabla \cdot \mathbf{J}_{\text{sur}}$  in  $S\text{-}T$  coordinates during February and August for comparison. An interesting difference between the 2 months is that the water mass formation and destruction that occur in temperatures lower than approximately  $20^\circ\text{C}$  is focused in one central band during August and in two central bands during February. This indicates that water mass formation and destruction is dominated by the winter hemisphere and reflects the fact that it occurs in two distinctly different basins during northern winter.

The different formation and destruction regions in  $S\text{-}T$  space, shown in Fig. 12, often correspond to

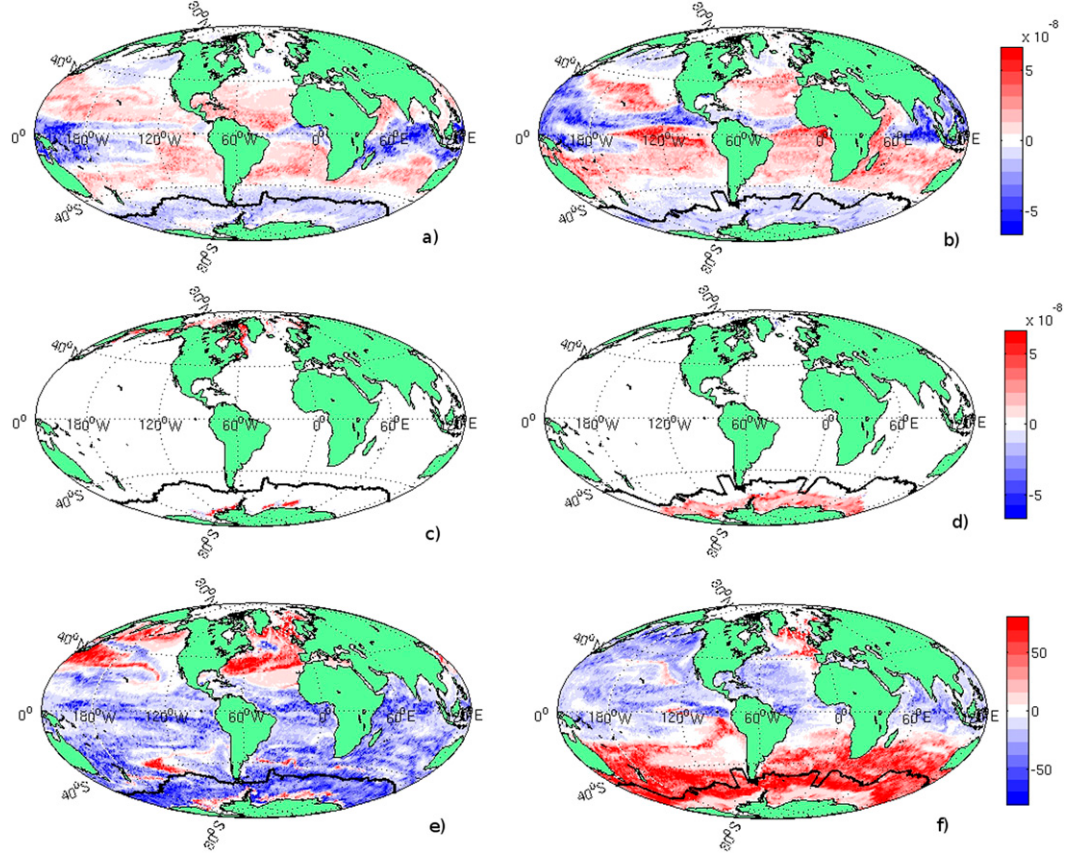


FIG. 11. Freshwater and heat fluxes projected from  $S-T$  coordinates into geographical coordinates. (left) February values and (right) August values. (a),(b) The net freshwater flux from precipitation, evaporation, and runoff ( $m s^{-1}$ ), (c),(d) net freshwater flux due to sea ice formation and melt ( $m s^{-1}$ ), and (e),(f) the net surface heat flux ( $W m^{-2}$ ).

geographically distinct regions in Fig. 10. For example, the convergence of  $\mathbf{J}_{\text{sur}}$  in the warmest part of Fig. 12 corresponds to the large blue formation zones in the western tropical Pacific and the northern Indian Ocean in Fig. 10. These formation zones coincide with large zones of excess precipitation shown in Figs. 11a and 11b.

In the coldest water just around the freezing point there is a dipole structure, with convergence in the coldest water and divergence in the slightly warmer water, both in the February and in the August panels of Fig. 12. The corresponding patterns in Fig. 10 are the red and blue areas around the coast of Antarctica for the August case

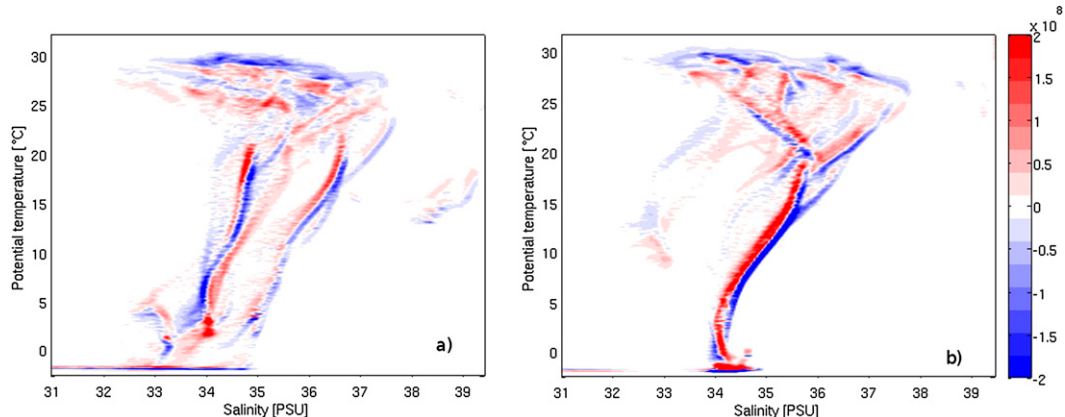


FIG. 12. Divergence of  $\mathbf{J}_{\text{sur}}$ . (a) February average and (b) August average, both in units of  $\text{m}^3(\text{psu } ^\circ\text{C s})^{-1}$ .

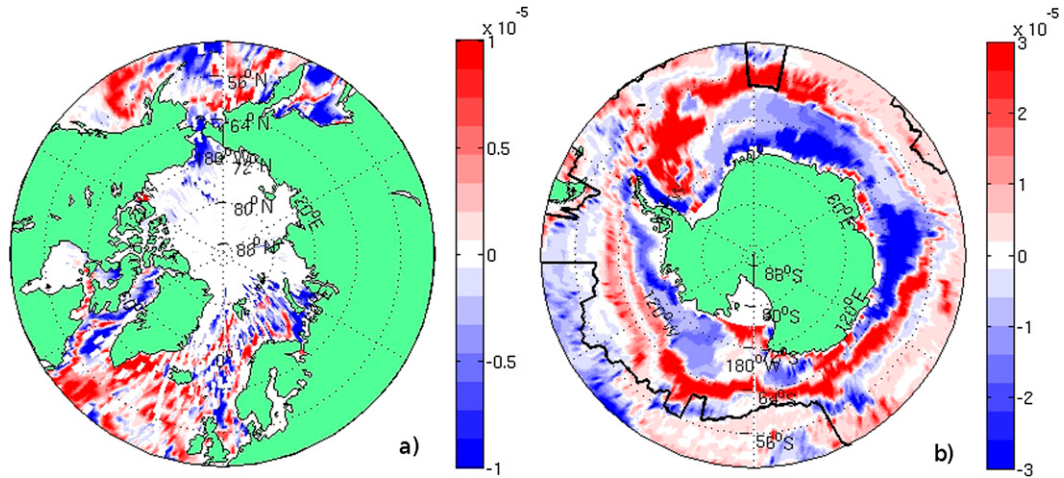


FIG. 13. High-latitude winter hemisphere water mass formation. (a) February average of  $\mathcal{F}(x, y, t)$  and (b) August average of  $\mathcal{F}(x, y, t)$ , both in units of  $\text{m s}^{-1}$ .

and the formation and destruction zones in the northern North Atlantic and Arctic for the February case. The high-latitude formation zones coincide with zones of strong freshwater forcing due to sea ice formation, as can be seen in Figs. 11c and 11d. Figure 13 offers a closeup of the water mass formation at high latitudes in the winter hemisphere. February is shown in Fig. 13a and August is shown in Fig. 13b. In this figure we can see that there is strong formation almost everywhere along the coast of Antarctica in the model, whereas in the Arctic formation occurs mostly around Bering Strait, Barents Sea, and around Baffin Bay and Davis Strait.

It was pointed out to us by Jan Zika (2014, personal communication) that the diagnostics of  $\mathbf{J}_{\text{sur}}$  (Fig. 5) and the freshwater fluxes shown in Fig. 11 explain why the diathermohaline streamfunction has three cells. It is clear from the diagnostics that the warmest waters in the ocean undergo freshening (due to the net precipitation in the warm pool), the waters between about  $10^\circ$  and  $28^\circ\text{C}$  typically undergo salinization (due to net evaporation in the subtropics and the remaining tropics), the cooler waters mostly undergo freshening (due to polar and subpolar net precipitation), and the coldest waters become more saline due to brine rejection. This clearly explains why there is an anticlockwise tropical cell, a clockwise conveyor belt cell, and an anticlockwise high-latitude or AABW cell. Importantly, this picture suggests that evaporation in the tropics and subtropics ultimately influences salinity of the dense NADW. This is also hinted at briefly in Zika et al. (2013).

The large divergence zone in the ACC seen in Fig. 10a (the February case) is mostly located just south of the black line that marks the position of the maximum wind speed, which approximately coincides with the maximum

northward Ekman transport. Speer et al. (2000) found that the transformation rate between density classes and the northward Ekman transport agreed well south of the line of maximum northward Ekman transport in the ACC. The water mass destruction south of this line is therefore expected because of the divergence in the Ekman transport. North of the line of maximum northward Ekman transport, Speer et al. (2000) found no good agreement between the transformation rate and the Ekman transport. In our case there are some areas of convergence just north of the maximum wind stress line in the February case, but the agreement is less striking than south of the line. During August (Fig. 10b) there is typically divergence both north and south of the maximum windstress line.

## 5. Conclusions

We have presented a framework for water mass analysis in  $S-T$  coordinates that is an extension of earlier work by Walin (1977, 1982) and Speer (1993) to include also water mass transformations in the interior ocean forced by mixing. Although we use salinity-temperature coordinates in our presentation, this framework can with equal ease be applied to any two conservative tracers. It is also shown how the transformation vector  $\mathbf{J}$ , which is discussed in this paper, relates to the diathermohaline streamfunction (Zika et al. 2012; Döös et al. 2012; Groeskamp et al. 2014). More specifically, our framework can be used to investigate how the cross-isothermal and cross-isohaline flows depicted by this streamfunction are driven by diabatic processes, both internally and at the ocean-atmosphere interface. We are also able to study the effects of different processes, for example, dianeutral and isoneutral diffusion separately. This sort of

separation was also done by Iudicone et al. (2008b) in their analysis of water mass transformations in a neutral density framework. A neutral density framework has both advantages and disadvantages as compared to one that uses salinity–temperature space. An obvious advantage of the salinity–temperature approach is that the resulting two-dimensional picture contains more details than a one-dimensional one; another is that salinity and temperature are much more accurately conserved than neutral density. A disadvantage of the  $S$ – $T$  approach is that our variables are not as dynamically relevant as neutral density; it is, for example, impossible to accurately distinguish diapycnal from isopycnal flow in  $S$ – $T$  space, unless the flow is along a known isobaric surface.

Two different circulation cells were found in our analysis of the  $\mathbf{J}$  vector (Fig. 5). These cells are similar to the tropical and conveyor belt cells found by Döös et al. (2012) and Zika et al. (2012) in their respective analyses of the thermohaline streamfunction. Both cells were found to have distinct Atlantic and Indo-Pacific branches, where the Atlantic branches occur at similar temperatures, but at higher salinities than the corresponding Pacific branches. The forcing of the two cells is different. The water mass transformation in the warm and shallow tropical cell is forced by surface fluxes and dianeutral diffusion, while the transformation in the conveyor belt cell is also highly influenced by isoneutral diffusion.

Another interesting result is that water mass transformation due to surface fluxes tend to be directed away from  $S$ – $T$  regions that occupy large areas at the sea surface. The surface fluxes thus tend to remove waters in the  $S$ – $T$  classes with large areal extent at the sea surface.

It was also shown how the divergence of the vector  $\mathbf{J}$  relates to water mass formation and how this can be used to study the effects of the different diabatic processes on the formation and destruction of different water masses. The ability to study water mass transformation due to different processes individually makes this framework a useful addition to the diathermohaline streamfunction as a diagnostic tool for water mass transformations in ocean models. The framework is, for example, well suited for comparing how different mixing parameterizations affect the water mass distribution in  $S$ – $T$  space. Furthermore, the use of  $S$ – $T$  coordinates is common in observational oceanography, so perhaps this framework can be the basis of fruitful cooperation between modellers and observationalists.

**Acknowledgments.** This work was financed by the Swedish Research Council, Grant 2008-4400. We also thank Kristofer Döös, Jan Zika, Sjoerd Groeskamp, and Daniele Iudicone for valuable discussions and insightful comments on the manuscripts. The representation of the

transformation vector given in Eq. (17) and in appendix C results from discussions with George Nurser during Ocean Sciences Meeting 2014. The simulations were performed on resources provided by the Swedish National Infrastructure for Computing (SNIC) at National Supercomputing Centre (NSC), Linköping.

## APPENDIX A

### Discretization of the Cross-Isothermal and Cross-Isohaline Fluxes

As defined,  $F_T(S, T, t)$  and  $F_S(S, T, t)$  are the fluxes through  $I_S(S, T, t)$  and  $I_T(S, T, t)$  of heat and salt, respectively (see Fig. 1). In a continuous manner, the time average  $F_T(S, T)$  can be written as

$$F_T(S, T) = \frac{1}{t_1 - t_0} \int_{t_0}^{t_1} \left( \int_{I_S} \boldsymbol{\phi}_T \cdot \mathbf{n}_{I_S} dA_{I_S} + \int_{I_T} \boldsymbol{\phi}_T \cdot \mathbf{n}_{I_T} dA_{I_T} \right) dt, \quad (\text{A1})$$

where  $t_1 - t_0$  is the evaluation period (26 yr in our case);  $\boldsymbol{\phi}_T$  is the nonadvective heat flux in the model;  $\mathbf{n}_{I_S}$  and  $\mathbf{n}_{I_T}$  are unit vectors normal to  $I_S$  and  $I_T$ , respectively; and  $dA_{I_S}$  and  $dA_{I_T}$  are area elements on  $I_S$  and  $I_T$ , respectively. Using the Gauss divergence theorem, Eq. (A1) can be written as

$$F_T(S, T) = \frac{1}{t_1 - t_0} \int_{t_0}^{t_1} \int_V \nabla \cdot \boldsymbol{\phi}_T dV dt, \quad (\text{A2})$$

with the discrete analog

$$F_T(S, T) = \frac{1}{t_1 - t_0} \sum_{t_0}^{t_1} \sum_i \sum_j \sum_k \nabla \cdot \boldsymbol{\phi}_T \Delta V \Delta t, \quad (\text{A3})$$

where  $\nabla \cdot \boldsymbol{\phi}_T$  is the discrete representation of the heat flux divergence, and  $i, j$ , and  $k$  are our coordinate directions ( $x, y, z$ ). To calculate Eq. (A3), we start by defining equidistant discrete representations of  $S$  and  $T$  with step lengths  $\Delta S$  and  $\Delta T$ . These discrete representations then form our  $S$ – $T$  space. We create separate  $S$ – $T$  matrices, two for each physical process, where one holds the heat fluxes and the other holds the salinity fluxes. For example, we have two matrices representing dianeutral diffusion and another two representing isoneutral diffusion. In this example we will use isoneutral diffusion, but all fluxes are calculated in the same way. We call the matrix containing the heat flux divergence from isoneutral diffusion  $\mathbf{M}_T^{\text{iso}}$ .

Since this is done online and in parallel on multiple processors, we save communication time by calculating

flux divergences on each processor separately and then adding up the result after the integration has finished. This means that we have  $n$  different matrices  $\mathbf{M}_T^{\text{iso}}$ , one for each processor. We start our calculation at every time step by looping over all grid boxes. For every grid box we

calculate the flux divergence due to each physical process and add it times  $\Delta V$  (the volume of the grid box) times  $\Delta t$  (the length of the time step) to the position in its respective matrix, where the grid box  $S$  and  $T$  values best match those in our discrete representation.  $\mathbf{M}_T^{\text{iso}}(S, T)$  is thus given by

$$\mathbf{M}_T^{\text{iso}}(S, T) = \sum_i \sum_j \sum_k \mathbf{V} \cdot \boldsymbol{\phi}_T^{\text{iso}} \mu[S - S(i, j, k)] \mu[T - T(i, j, k)] \Delta V \Delta t, \quad (\text{A4})$$

where,

$$\mu(\sigma) = \begin{cases} 1, & |\sigma| < \Delta T/2 \\ 0 & \text{otherwise} \end{cases}. \quad (\text{A5})$$

The sampling function for salinity is defined in the same way, but using  $\Delta S/2$ .

After the integration has finalized, we add the matrices that contain integrated flux divergences due to the same physical process, but were produced by different processors together and divide by  $t_1 - t_0$  (the time of integration). We now have only two matrices,  $\mathbf{M}$ , per process. Since we have the flux divergences stored process by process, we can identify the flux from each process, and  $F_T$  is simply given by summation over  $\mathbf{M}$ :

$$F_T^{\text{iso}}(S, T) = \sum_{-\infty}^S \sum_{-\infty}^T \mathbf{M}_{\text{iso}}(S, T). \quad (\text{A6})$$

Now since

$$cG_T^{\text{iso}} = -\frac{\partial F_T^{\text{iso}}}{\partial T}, \quad (\text{A7})$$

and

$$G_S^{\text{iso}} = -\frac{\partial F_S^{\text{iso}}}{\partial S}, \quad (\text{A8})$$

we get a simple expression for the  $\mathbf{J}_{\text{iso}}$  vector according to

$$\begin{aligned} \mathbf{J}_{\text{iso}} &= \left( \frac{\partial G_S^{\text{iso}}}{\partial T}, \frac{\partial G_T^{\text{iso}}}{\partial S} \right) = \left( -\frac{\partial^2 F_S^{\text{iso}}}{\partial T \partial S}, -\frac{1}{c} \frac{\partial^2 F_T^{\text{iso}}}{\partial T \partial S} \right) \\ &= -\left( \frac{\mathbf{M}_S^{\text{iso}}(S, T)}{\Delta S \Delta T}, \frac{\mathbf{M}_T^{\text{iso}}(S, T)}{c \Delta S \Delta T} \right). \end{aligned} \quad (\text{A9})$$

## APPENDIX B

### The Thermohaline and the Diathermohaline Streamfunction

The volume flows  $G_T$  and  $G_S$  can, in a steady state, be used to define the diathermohaline streamfunction of

[Groeskamp et al. \(2014\)](#) [see Eq. (23)]. This streamfunction represents the net transports across property surfaces that may move in space. Accordingly, it is the difference between the fluid velocity and the velocity of the property surfaces that determine these flows, see also [Iudicone et al. \(2011\)](#). The thermohaline streamfunction ([Zika et al. 2012; Döös et al. 2012](#)) as first defined, however, was treating the property surfaces as fixed in space. In what follows we will illustrate the difference.

The velocity of an isothermal surface normal to itself ( $\mathbf{u}_T$ ), is defined through (e.g., [Marshall et al. 1999](#))

$$\frac{\partial T}{\partial t} + \mathbf{u}_T \cdot \nabla T = 0, \quad (\text{B1})$$

where  $T$  here represents the spatial and temporal temperature distribution. Thus, the velocity of an isothermal surface can be written as

$$\mathbf{u}_T = -\frac{\partial T}{\partial t} \frac{\nabla T}{|\nabla T|^2}. \quad (\text{B2})$$

The flow  $G_T$  that represents water mass transformation can be calculated as

$$G_T(S, T, t) = \iint_{I_T} (\mathbf{u} - \mathbf{u}_T) \cdot dA, \quad (\text{B3})$$

where  $dA$  is the area element on  $I_T$  pointing toward increasing temperature. In a steady state,  $G_T$  is the diathermohaline streamfunction. The thermohaline streamfunction on the other hand is calculated assuming  $\mathbf{u}_T = 0$ . Equation (B3) is a purely kinematical relation; using Eq. (2), it can be written as

$$G_T(S, T, t) = -\frac{1}{c} \iint_{I_T} \frac{\nabla \cdot \boldsymbol{\phi}_T}{|\nabla T|} dA. \quad (\text{B4})$$

An alternative way of defining the respective streamfunctions is by considering the volume transport through an isohaline surface. By introducing the velocity of isohaline surfaces  $\mathbf{u}_S$ , defined analogously to  $\mathbf{u}_T$  in Eq. (B2), the flow penetrating the isohaline surface  $I_S$  can be written as

$$G_S(S, T, t) = \iint_{I_S} (\mathbf{u} - \mathbf{u}_S) \cdot dA, \quad (\text{B5})$$

where  $dA$  is the area element on  $I_S$  pointing toward increasing salinity. Analogously to the case with  $G_T$ , the thermohaline streamfunction is calculated by assuming  $\mathbf{u}_S = 0$ . By using Eq. (3) one arrives at

$$G_S(S, T, t) = -\iint_{I_S} \frac{\nabla \cdot \phi_S}{|\nabla S|} dA. \quad (\text{B6})$$

[Groeskamp et al. \(2014\)](#) calculates the diathermohaline streamfunction by separately calculating the thermohaline streamfunction, and what they call the local thermohaline streamfunction (the part related to  $\mathbf{u}_T$  or  $\mathbf{u}_S$ ). The diathermohaline streamfunction from our run is dominated by the contribution from the thermohaline streamfunction. A noteworthy exception is the anticlockwise (blue) cell occurring in subzero temperatures approximately between salinities of 34 and 34.5 psu, which is almost completely due to the local thermohaline streamfunction (i.e., the part related to  $\mathbf{u}_T$  or  $\mathbf{u}_S$ ). The local part also helps to amplify the tropical cell.

## APPENDIX C

### A Different View of the Transformation Vector

A physically illuminating definition of the vector  $\mathbf{J}$  can be derived from Eq. (B6):

$$G_S(S, T, t) = -\iint_{I_S} \frac{\nabla \cdot \phi_S}{|\nabla S|} dA.$$

Using Reynolds transport theorem on Eq. (B6) gives

$$G_S(S, T, t) = -\frac{\partial}{\partial S} \iiint_{V(S, T, t)} \nabla \cdot \phi_S dV. \quad (\text{C1})$$

Using Eq. (3), Eq. (C1) may be written as

$$G_S(S, T, t) = \frac{\partial}{\partial S} \iiint_{V(S, T, t)} \frac{DS}{Dt} dV. \quad (\text{C2})$$

Differentiating Eq. (C2) with respect to  $T$  gives

$$\frac{\partial G_S(S, T, t)}{\partial T} = \frac{\partial}{\partial T} \frac{\partial}{\partial S} \iiint_{V(S, T, t)} \frac{DS}{Dt} dV, \quad (\text{C3})$$

which can also be written as

$$\frac{\partial G_S(S_0, T_0, t)}{\partial T} = \lim_{\Delta S \rightarrow 0, \Delta T \rightarrow 0} \frac{1}{\Delta T \Delta S} \iiint_{\Delta V(S_0, T_0, t)} \frac{DS}{Dt} dV. \quad (\text{C4})$$

where  $\Delta V(S_0, T_0, t)$  is the volume of ocean water with  $S \in [S_0, S_0 + \Delta S]$  and  $T \in [T_0, T_0 + \Delta T]$ . The same manipulations applied to Eq. (B4) gives

$$\frac{\partial G_T(S_0, T_0, t)}{\partial S} = \lim_{\Delta S \rightarrow 0, \Delta T \rightarrow 0} \frac{1}{\Delta T \Delta S} \iiint_{\Delta V(S_0, T_0, t)} \frac{DT}{Dt} dV, \quad (\text{C5})$$

We now define

$$\dot{S}\nu \equiv \lim_{\Delta S \rightarrow 0, \Delta T \rightarrow 0} \frac{1}{\Delta T \Delta S} \iiint_{\Delta V(S_0, T_0, t)} \frac{DS}{Dt} dV \quad (\text{C6})$$

and

$$\dot{T}\nu \equiv \lim_{\Delta S \rightarrow 0, \Delta T \rightarrow 0} \frac{1}{\Delta T \Delta S} \iiint_{\Delta V(S_0, T_0, t)} \frac{DT}{Dt} dV, \quad (\text{C7})$$

where  $\nu$  is defined in Eq. (4), and  $\dot{T}(\dot{S})$  is the net heating (salinization) of  $\Delta V$ . The transformation vector  $\mathbf{J}$  defined in Eq. (16) can now be written as

$$\mathbf{J} = \nu(\dot{S}, \dot{T}). \quad (\text{C8})$$

## REFERENCES

- Antonov, J. I., R. A. Locarnini, T. P. Boyer, A. V. Mishonov, and H. E. Garcia, 2006: *Salinity*. Vol. 2, *World Ocean Atlas 2005*, NOAA Atlas NESDIS 62, 182 pp.
- Beckmann, A., and R. Dösscher, 1997: A method for improved representation of dense water spreading over topography in geopotential-coordinate models. *J. Phys. Oceanogr.*, **27**, 581–591, doi:[10.1175/1520-0485\(1997\)027<0581:AMFIRO>2.0.CO;2](https://doi.org/10.1175/1520-0485(1997)027<0581:AMFIRO>2.0.CO;2).
- Brambilla, E., L. D. Talley, and P. E. Robbins, 2008: Subpolar mode water in the northeastern Atlantic: 2. Origin and transformation. *J. Geophys. Res.*, **113**, C04026, doi:[10.1029/2006JC004063](https://doi.org/10.1029/2006JC004063).
- Brodeau, L., B. Barnier, A. M. Treguier, T. Penduff, and S. Gulev, 2010: An ERA40-based atmospheric forcing for global ocean circulation models. *Ocean Model.*, **31**, 88–104, doi:[10.1016/j.ocemod.2009.10.005](https://doi.org/10.1016/j.ocemod.2009.10.005).
- Bryan, K., and J. L. Sarmiento, 1985: Modeling ocean circulation. *Advances in Geophysics*, Vol. 28, Academic Press, 433–459, doi:[10.1016/S0065-2687\(08\)60232-0](https://doi.org/10.1016/S0065-2687(08)60232-0).
- Burchard, H., and H. Rennau, 2008: Comparative quantification of physically and numerically induced mixing in ocean models. *Ocean Model.*, **20**, 293–311, doi:[10.1016/j.ocemod.2007.10.003](https://doi.org/10.1016/j.ocemod.2007.10.003).
- Döös, K., J. Nilsson, J. Nylander, L. Brodeau, and M. Ballarotta, 2012: The world ocean thermohaline circulation. *J. Phys. Oceanogr.*, **42**, 1445–1460, doi:[10.1175/JPO-D-11-0163.1](https://doi.org/10.1175/JPO-D-11-0163.1).
- Emery, W., and J. Meincke, 1986: Global water masses: Summary and review. *Oceanol. Acta*, **9**, 383–391.
- Ferrari, R., and D. Ferreira, 2011: What processes drive the ocean heat transport. *Ocean Model.*, **38**, 171–186, doi:[10.1016/j.ocemod.2011.02.013](https://doi.org/10.1016/j.ocemod.2011.02.013).
- Fichefet, T., and M. M. Maqueda, 1997: Sensitivity of a global sea ice model to the treatment of ice thermodynamics and dynamics. *J. Geophys. Res.*, **102**, 12 609–12 646, doi:[10.1029/97JC00480](https://doi.org/10.1029/97JC00480).

- Gaspar, P., Y. Groris, and J.-M. Lefevre, 1990: A simple eddy kinetic energy model for simulations of the oceanic vertical mixing: Tests at station Papa and long-term upper ocean study site. *J. Geophys. Res.*, **95**, 16 179–16 193, doi:10.1029/JC095iC09p16179.
- Gent, P. R., and J. C. McWilliams, 1990: Isopycnal mixing in ocean circulation models. *J. Phys. Oceanogr.*, **20**, 150–155, doi:10.1175/1520-0485(1990)020<0150:IMIOCM>2.0.CO;2.
- Groeskamp, S., J. D. Zika, T. J. McDougall, B. M. Sloyan, and F. Laliberté, 2014: The representation of ocean circulation and variability in thermodynamic coordinates. *J. Phys. Oceanogr.*, **44**, 1735–1750, doi:10.1175/JPO-D-13-0213.1.
- Hieronymus, M., and J. Nylander, 2013a: The budgets of heat and salinity in NEMO. *Ocean Modell.*, **67**, 28–38, doi:10.1016/j.ocemod.2013.03.006.
- , and —, 2013b: The buoyancy budget with a nonlinear equation of state. *J. Phys. Oceanogr.*, **43**, 176–186, doi:10.1175/JPO-D-12-063.1.
- Hirst, A. C., D. R. Jackett, and T. J. McDougall, 1996: The meridional overturning cells of a world ocean model in neutral coordinates. *J. Phys. Oceanogr.*, **26**, 775–791, doi:10.1175/1520-0485(1996)026<0775:TMOCOA>2.0.CO;2.
- Iudicone, D., G. Madec, B. Blanke, and S. Speich, 2008a: The role of Southern Ocean surface forcing and mixing in the global conveyor. *J. Phys. Oceanogr.*, **38**, 1377–1400, doi:10.1175/2008JPO3519.1.
- , —, and T. J. McDougall, 2008b: Water-mass transformation in a neutral density framework and the key role of light penetration. *J. Phys. Oceanogr.*, **38**, 1357–1376, doi:10.1175/2007JPO3464.1.
- , K. B. Rodgers, I. Stendardo, O. Aumont, G. Madec, L. Bopp, O. Mangoni, and M. Ribera, 2011: Water masses as a unifying framework for understanding the Southern Ocean carbon cycle. *Biogeosciences*, **8**, 1031–1052, doi:10.5194/bg-8-1031-2011.
- Kjellsson, J., K. Döös, F. B. Lalibert, and J. D. Zika, 2014: The atmospheric general circulation in thermodynamical coordinates. *J. Atmos. Sci.*, **71**, 916–928, doi:10.1175/JAS-D-13-0173.1.
- Locarnini, R. A., A. V. Mishonov, J. I. Antonov, T. P. Boyer, and H. E. Garcia, 2006: *Temperature*. Vol. 1, *World Ocean Atlas 2005*, NOAA Atlas NESDIS 61, 182 pp.
- Luyten, J. R., J. Pedlosky, and H. Stommel, 1983: The ventilated thermocline. *J. Phys. Oceanogr.*, **13**, 292–309, doi:10.1175/1520-0485(1983)013<0292:TVT>2.0.CO;2.
- Madec, G., 2008: NEMO ocean engine. Note du Pôle de Modélisation de l'Institut Pierre-Simon Laplace 27, 217 pp. [Available online at [http://www.nemo-ocean.eu/content/download/5302/31828/file/NEMO\\_book.pdf](http://www.nemo-ocean.eu/content/download/5302/31828/file/NEMO_book.pdf).]
- , P. Delecluse, M. Imbard, and C. Levy, 1998: OPA 8.1 ocean general circulation model: Reference manual. Note du Pole de Modlisation de l'Institut Pierre-Simon Laplace 11, 97 pp. [Available online at [http://www.nemo-ocean.eu/Media/Files/Doc\\_OPA8.1](http://www.nemo-ocean.eu/Media/Files/Doc_OPA8.1).]
- Maqueda, M. A. M., and G. Holloway, 2006: Second-order moment advection scheme applied to Arctic Ocean simulation. *Ocean Modell.*, **14**, 197–221, doi:10.1016/j.ocemod.2006.05.003.
- Marshall, D., 1997: Subduction of water masses in an eddying ocean. *J. Mar. Res.*, **55**, 201–222, doi:10.1357/0022240973224373.
- Marshall, J., and G. Nurser, 1991: A continuously stratified thermocline model incorporating a mixed layer of variable thickness and density. *J. Phys. Oceanogr.*, **21**, 1780–1792, doi:10.1175/1520-0485(1991)021<1780:ACSTMI>2.0.CO;2.
- , and K. Speer, 2012: Closure of the meridional overturning circulation through Southern Ocean upwelling. *Nat. Geosci.*, **5**, 171–180, doi:10.1038/ngeo1391.
- , J. D. Jamous, and J. Nilsson, 1999: Reconciling thermodynamic and dynamic methods of computation of water-mass transformation rates. *Deep-Sea Res.*, **46**, 545–572, doi:10.1016/S0967-0637(98)00082-X.
- Maze, G., G. Forget, M. Buckley, J. Marshall, and I. Cerovecki, 2009: Using transformation and formation maps to study the role of air-sea heat fluxes in North Atlantic Eighteen Degree Water formation. *J. Phys. Oceanogr.*, **39**, 1818–1835, doi:10.1175/2009JPO3985.1.
- Munk, W. H., 1966: Abyssal recipes. *Deep-Sea Res. Oceanogr. Abstr.*, **13**, 707–730, doi:10.1016/0011-7471(66)90602-4.
- Nikurashin, M., and G. K. Vallis, 2012: A theory of the interhemispheric meridional overturning circulation and associated stratification. *J. Phys. Oceanogr.*, **42**, 1652–1667, doi:10.1175/JPO-D-11-0189.1.
- Nilsson, J., 1996: Mixing in the ocean produced by tropical cyclones. *Tellus*, **48A**, 342–355, doi:10.1034/j.1600-0870.1996.t01-1-00010.x.
- , and H. Körnich, 2008: A conceptual model of the surface salinity distribution in the oceanic Hadley cell. *J. Climate*, **21**, 6586–6598, doi:10.1175/2008JCLI2284.1.
- Paulson, C. A., and J. Simpson, 1977: Irradiance measurements in the upper ocean. *J. Phys. Oceanogr.*, **7**, 952–956, doi:10.1175/1520-0485(1977)007<0952:IMTUO>2.0.CO;2.
- Picard, G. L., and W. J. Emery, 1982: *Descriptive Physical Oceanography*. 4th ed. Pergamon Press, 249 pp.
- Redi, M. H., 1982: Oceanic isopycnal mixing by coordinate rotation. *J. Phys. Oceanogr.*, **12**, 1154–1158, doi:10.1175/1520-0485(1982)012<1154:OIMBCR>2.0.CO;2.
- Simmons, H. L., S. R. Jayne, L. C. S. Laurent, and A. J. Weaver, 2004: Tidally driven mixing in a numerical model of the ocean general circulation. *Ocean Modell.*, **6**, 245–263, doi:10.1016/S1463-5003(03)00011-8.
- Speer, K. G., 1993: Conversion among North Atlantic surface water types. *Tellus*, **45A**, 72–79, doi:10.1034/j.1600-0870.1993.00006.x.
- , and E. Tziperman, 1992: Rates of water mass formation in the North Atlantic Ocean. *J. Phys. Oceanogr.*, **22**, 93–104, doi:10.1175/1520-0485(1992)022<0093:ROWMFI>2.0.CO;2.
- , S. R. Rintoul, and B. Sloyan, 2000: The diabatic Deacon cell. *J. Phys. Oceanogr.*, **30**, 3212–3222, doi:10.1175/1520-0485(2000)030<3212:TDDC>2.0.CO;2.
- Swift, J. H., 1984: The circulation of the Denmark Strait and Iceland-Scotland overflow waters in the North Atlantic. *Deep-Sea Res.*, **31**, 1339–1355, doi:10.1016/0198-0149(84)90005-0.
- Tziperman, E., 1986: On the role of interior mixing and air-sea fluxes in determining the stratification and circulation of the ocean. *J. Phys. Oceanogr.*, **16**, 680–692, doi:10.1175/1520-0485(1986)016<0680:OTROIM>2.0.CO;2.
- Walsh, G., 1977: A theoretical framework for the description of estuaries. *Tellus*, **29**, 128–136, doi:10.1111/j.2153-3490.1977.tb00716.x.
- , 1982: On the relation between sea-surface heat flow and the thermal circulation in the ocean. *Tellus*, **34**, 187–195, doi:10.1111/j.2153-3490.1982.tb01806.x.
- Welander, P., 1959: An advective model of the ocean thermocline. *Tellus*, **11**, 309–318, doi:10.1111/j.2153-3490.1959.tb00036.x.
- Wijffels, S. E., R. W. Schmitt, H. L. Bryden, and A. Stigebrandt, 1992: Transport of freshwater by the oceans. *J. Phys. Oceanogr.*, **22**, 155–162, doi:10.1175/1520-0485(1992)022<0155:TOFBTO>2.0.CO;2.
- Worthington, L. V., 1981: The water masses of the world ocean: Some results of a fine-scale census. *Evolution of Physical Oceanography*, MIT Press, 42–69.
- Zika, J. D., M. H. England, and W. P. Sijp, 2012: The ocean circulation in thermohaline coordinates. *J. Phys. Oceanogr.*, **42**, 708–724, doi:10.1175/JPO-D-11-0139.1.
- , W. P. Sijp, and M. H. England, 2013: Vertical heat transport by ocean circulation and the role of mechanical and haline forcing. *J. Phys. Oceanogr.*, **43**, 2095–2112, doi:10.1175/JPO-D-12-0179.1.